Exotic Quantum States of Circuit Quantum Electrodynamics in the Ultra-Strong Coupling Regime

Mahn-Soo Choi

The quantum coherent behaviors of superconducting devices at macroscopic scales and recent technical advances in fine tunability have brought the conventional cavity quantum electrodynamics (QED) to superconducting circuits. With an ultra-strong cavity photon–artificial atom coupling and the inherent nonlinearity of the Josephson junctions, the so-called circuit QED offers new opportunities to explore new realms of physics that have remained a challenge for conventional cavity QED. Circuit QED has even attracted public attention as the leading architecture for quantum computation. In this article, a pedagogical review of recent studies and activities on exotic quantum states that can be attributed to ultra-strong coupling is provided. A progress report on attempts to seek the smallest unit of the topological matter and its fundamental interaction with light is also provided.

1. Introduction

Roughly speaking and according to our current understanding, the universe consists of energy (possibly including dark energy) and matter (possibly including dark matter). Light is representative of energy while matter is composed of atoms. The light–atom interaction has naturally attracted significant attention from the general public. One particular system is notable: the cavity quantum electrodynamics (QED) system. It is a minimal system where "photons", or light quanta, confined inside the cavity interact with "qubits", two-level quantum systems, that serve as the smallest unit of atoms (hence matter). Despite the simplicity of the cavity QED system, it contains all essential ingredients regarding the light–matter interaction. On that account, it is no wonder that ever since the early age of quantum mechanics, the cavity QED systems have been the subject of a vast amount of research. They have revealed many intriguing features of the light–matter interaction as well as quantized light and quantum matter themselves. However, conventional cavity QED systems bear two important drawbacks: first, the photon–qubit coupling is too weak and (as illustrated recently in other architectures with ultra-strong coupling) the observable physical effects are rather limited. Second and more importantly, the usual qubit does not

Prof. M.-S. Choi
Department of Physics
Korea University
Seoul 02841, Republic of Korea
E-mail: choims@korea.ac.kr

The ORCID identification number(s) for the author(s) of this article can be found under https://doi.org/10.1002/qute.202000085

properly represent the topological matter, which has risen as a major topic in the field of condensed-matter physics.

The resolution to weak photon–qubit coupling has come from an unprecedented architecture based on superconducting circuits. The so-called superconducting circuit QED system (see **Figure 1**) is a planar superconducting transmission line of a few centimeters in length that interacts electrically and/or magnetically with superconducting qubits embedded within it. As pointed out in ref. [1] and soon after demonstrated experimentally in ref. [2], the small effective mode volume makes microwave photon–qubit coupling in the circuit QED systems very strong. Such an ultra-strong coupling provides an outstanding platform for various exotic strong-coupling quantum effects[3] that would have been elusive in conventional cavity QED systems. In Sections 2–7, we will provide a pedagogical review of the recent developments and activities concerning the fundamental ultra-strong coupling effects in circuit QED that are difficult to observe in conventional cavity QED.

On the other hand, even the circuit QED systems studied so far involve usual qubits exploiting no topological characteristics. Recently, there have been some valuable attempts to couple Majorana Fermion modes in topological superconductors with a circuit resonator[4,5]; see also Section 9. Unfortunately, however, the coupling strength is small, and most activities have focused on examining new experimental tools to probe certain specific topological properties.

A natural question at this stage is: What is the smallest unit (if any) of topological matter? That is, could one conceive of a simple yet quintessence-seizing model for the topological matter that will eventually reveal the fundamental principle of the light-topological matter interaction? Sections 8 and 9 are devoted to this issue and report on the progress of some attempts to seek answers to the question.
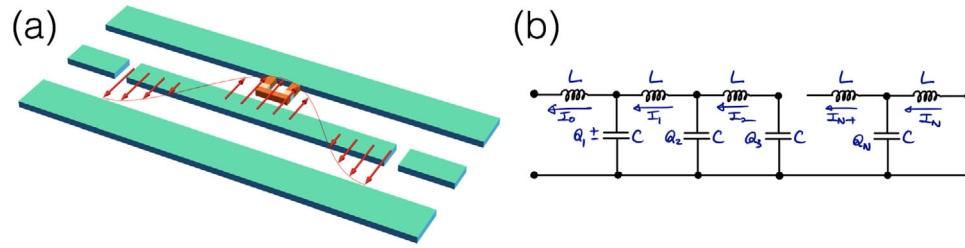
2. Circuit QED Systems

Circuit quantum electrodynamics (QED)[1,2,6] is a re-implementation of the atomic cavity QED[7,8] in superconducting circuits. It replaces the traditional optical cavity with a superconducting transmission line and the atoms with artificial atoms, that is, qubits. Unlike the typical cavity QED that involves millions or billions of atoms floating "in the space", the circuit QED deals with just a few qubits fixed inside circuit and provides greater tunability. Further, the coupling between the qubit and

ADVANCED
SCIENCE NEWS
www.advancedsciencenews.com

ADVANCED
QUANTUM
TECHNOLOGIES
www.advquantumtech.com

Figure 1. a) Schematic diagram of the circuit quantum electrodynamics (QED) system consisting of the superconducting circuit resonator (shown in cyan) and the superconducting qubit (in orange and white). The electromagnetic field (arrows in red) of the resonance mode (sine wave in red) along the central wire piece (a few centimeters long and a few nanometers wide) electrically and/or magnetically modulates the qubit parameters, and ultra strong coupling is accordingly achieved between the microwave photon and the qubit. The entangled photon–qubit states can be probed by means of microwave transmission and/or reflection through the input and output ports connected capacitively to the central resonator piece. The outermost superconducting plates are ground plates confining the electromagnetic wave within the trench. More details are present in ref. [1]. b) Equivalent circuit of the circuit QED system.

the cavity field is several thousand times larger (relative to the resonant frequency) than the one in cavity QED. These two factors and the other technical aspects allow the circuit QED to explore the regime that is difficult to reach in cavity QED. One of the main purposes of this article is to survey the studies of such exotic quantum regimes and their associated quantum states.

Of course, it should also be noted that combined with a long decoherence time of the transmon qubit,[9,10] the circuit QED has provided easily accessible experimental tools to process quantum information such that circuit QED has become one of the leading architectures for quantum computation. The public has got to regard superconducting quantum computers as realistic.[11] In this article, however, we will focus more on the quantum physics originating from the ultra-strong light–matter interaction rather than in the context of quantum information processing and scalable quantum computation, which is referred to ref. [12].

A circuit QED system consists of a superconducting circuit resonator and a superconducting qubit as is schematically shown in Figure 1. The resonator is typically centimeters long and surrounded by superconducting ground plates to prevent electromagnetic radiation loss. The qubit can be of any type, including charge,[13] flux,[14] and phase[15] qubits, but in most applications the so-called transmon qubits[9,10,16] are used due to their long decoherence time.

2.1. Quantization of the Resonator

For the cavity, a transmission line in the form of a coplanar wave guide[1,2] is the most common, but recently, a 3D cavity[17] has also been widely used. To simplify the discussion, here we focus on the coplanar wave guide.

The charge in the superconducting transmission line cannot remain still due to the zero-point quantum fluctuation effect, and its fluctuations propagate along the transmission line with the speed of light, microscopically governed by Maxwell's equations. Since the transmission line is centimeters long, the elementary modes are expected to have wavelengths of a similar scale. This means that it is enough to quantize the charge fluctuations at the macroscopic level in terms of the capacitance per unit length and the inductance per unit length of the transmission line. This is

the approach that is taken in ref. [1] and the charge fluctuations were described by a continuous field variable.

Here, we take a similar approach but discretize the transmission line of length ℓ into N segments. In this picture, the transmission line is equivalent to the circuit containing a series of capacitors and inductors; see Figure 1b. The Kirchhoff's law on each loop gives the relation

$$I_n = \sum_{j=1}^{n} \frac{dQ_j}{dt} \tag{1}$$

among the currents I_n through the inductors and the charge Q_n on the capacitors. The boundary conditions are

$$I_0 = I_N = 0 \tag{2}$$

from the fact that the circuit is open, and

$$Q_1 + Q_2 + \cdots + Q_N = 0 \tag{3}$$

from the charge neutrality. It is useful to define auxiliary variables

$$\Phi_0 = 0, \quad \Phi_n = \sum_{j=1}^{n} Q_j \quad (n = 1, 2, \ldots, N) \tag{4}$$

so that

$$Q_n = \Phi_n - \Phi_{n-1}, \quad I_n = \frac{d\Phi_n}{dt} \quad (n = 1, \ldots, N) \tag{5}$$

Note that the total charge neutrality condition gives

$$\Phi_N = 0 \tag{6}$$

The Lagrangian is given by

$$\mathcal{L} = \frac{1}{N} \sum_{n=1}^{N} \left[\frac{1}{2} L_r \dot{\Phi}_n^2 - \frac{(\Phi_n - \Phi_{n-1})^2}{2C_r} \right]$$

$$= \frac{1}{N} \sum_{n=1}^{N} \left[\frac{1}{2} L_r \dot{\Phi}_n^2 - \frac{1}{2} L_r \omega_{LC}^2 (\Phi_n - \Phi_{n-1})^2 \right] \tag{7}$$

ADVANCED
SCIENCE NEWS
www.advancedsciencenews.com

ADVANCED
QUANTUM
TECHNOLOGIES
www.advquantumtech.com

where C_r and L_r are the total capacitance and inductance, respectively, of the transmission line, and $\omega_{LC} := N/\sqrt{L_r C_r}$ is the LC frequency of each segment. Recall that $\Phi_0 = \Phi_N = 0$. The Lagrangian is formally the same as that of a loaded string. To find the normal modes, we take a discrete Fourier sine transform

$$\Phi_n = \sqrt{\frac{2}{N}} \sum_{m=1}^{N-1} \phi_m \sin\left(\frac{mn\pi}{N}\right) \quad (n = 1, \ldots, N-1) \tag{8}$$

upon which the Lagrangian is reduced to

$$\mathcal{L} = \frac{1}{N} \sum_{n=1}^{N-1} \left(\frac{1}{2} L_r \dot{\phi}_n^2 - \frac{1}{2} L_r \omega_n^2 \phi_n^2 \right) \tag{9}$$

with

$$\omega_n := 2\omega_{LC} \sin\left(\frac{n\pi}{2N}\right) \tag{10}$$

The corresponding Hamiltonian is given by

$$H = \sum_{n=1}^{N-1} \left[\frac{\pi_n^2}{2L_r/N} + \frac{1}{2}(L_r/N)\omega_n^2 \phi_n^2 \right] \tag{11}$$

where $\pi_n := (L_r/N)\dot{\phi}_n$ is the canonical momentum conjugate to ϕ_n. Obviously, it is a collection of simple Harmonic oscillators with natural frequencies ω_n.

So far the description is all classical. Now, we quantize the model by replacing the classical variables ϕ_n and π_n by the operators $\hat{\phi}_n$ and $\hat{\pi}_n$, respectively, which satisfy the canonical commutation relations

$$[\hat{\phi}_m, \hat{\pi}_n] = i\delta_{mn}. \tag{12}$$

Furthermore, we introduce the annihilation operator

$$\hat{a}_n := \frac{1}{\sqrt{2}} \left[\sqrt{\omega_n L_r/N} \hat{\phi}_n + i\hat{\pi}_n/\sqrt{\omega_n L_r/N} \right] \tag{13}$$

which satisfies the commutation relations

$$[\hat{a}_m, \hat{a}_n^\dagger] = \delta_{mn}, \quad [\hat{a}_m, \hat{a}_n] = [\hat{a}_m^\dagger, \hat{a}_n^\dagger] = 0 \tag{14}$$

Putting these together, we obtain the Hamiltonian

$$\hat{H}_{\text{cavity}} = \sum_{n=1}^{N-1} \omega_n \hat{a}_n^\dagger \hat{a}_n \tag{15}$$

In the continuum limit ($N \to \infty$), the normal-mode frequency ω_n in (10) is reduced to

$$\omega_n = vk_n \tag{16}$$

where $v := \ell/\sqrt{L_r C_r}$ is the "speed of light" and $k_n := \pi n/\ell$ is the wave number of the mode. With $\ell \approx 1$ cm, the frequency of the fundamental mode $\omega_1 \approx 5$ GHz. In applications, one chooses a particular mode ω_n and assumes the other modes are well separated and do not affect the system in question. In this regards,

from now on, we drop the subscript index for the mode of choice and simply write the mode frequency as ω.

The voltage due to the (quantized) cavity field is given by

$$\hat{V} = V_{\text{rms}}(\hat{a} + \hat{a}^\dagger) \tag{17}$$

with the root-mean-square value $V_{\text{rms}} = \sqrt{\omega/C_r}$ (we have put $\hbar = 1$).

2.2. Superconducting Qubits

Many hybrid systems have been experimentally realized with various quantum devices coupled to the superconducting resonator, including carbon nanowire quantum dots,[18] semiconductor spin qubits,[19] diamond nitrogen-vacancy color centers,[20] and many other of varying materials. Here, we will focus on the transmon qubit: the coupling of other types of qubits and quantum devices is essentially similar in the relevant low-energy regime.

A transmon qubit[9,10,16] is a Cooper box[13] with the relative magnitudes of Josephson and charging energies reversed. It is described by the Hamiltonian

$$\hat{H}_{\text{transmon}} = 4E_C(\hat{n} - n_g)^2 - E_J \cos\hat{\varphi} \tag{18}$$

where $E_C := e^2/2C$ is the charging energy of the superconducting island with a total capacitance C and E_J is the Josephson energy of the junction. The gate charge n_g (in units of the Cooper pair charge $2e$) is tuned via the gate voltage V_g across the gate capacitance C_g. The number of Cooper pairs, $\hat{n}$, and the superconducting phase difference between the superconducting island and reservoir, $\hat{\varphi}$, are canonical conjugates of each other satisfying the commutation relation

$$[\hat{n}, \hat{\varphi}] = i \tag{19}$$

In the large Josephson energy limit ($E_J \gg E_C$), the system described by the Hamiltonian (18) can be regarded as a harmonic oscillator with nonlinearity with $\hat{n}$ playing the role of the "position" and $\hat{\varphi}$ the momentum. In this limit, the nonlinearity is small (yet sufficiently large for two-level approximation, see below) which can be seen by expanding the "potential" (up to an irrelevant constant energy shift)

$$\hat{H}_{\text{transmon}} \approx 4E_C(\hat{n} - n_g)^2 + \frac{E_J}{2}\hat{\varphi}^2 - \frac{E_J}{24}\hat{\varphi}^4 + \cdots \tag{20}$$

Effectively, the Hamiltonian of the transmon qubit reads as

$$\hat{H}_{\text{transmon}} \approx \Omega \left[\hat{b}^\dagger\hat{b} - \frac{n_g\beta}{\sqrt{2}}(\hat{b} + \hat{b}^\dagger) - \frac{\beta}{16}\hat{b}^\dagger\hat{b}(\hat{b}^\dagger\hat{b} - 1) \right] \tag{21}$$

where $\hat{b} := (\sqrt{\beta}\hat{n} + i\hat{\varphi}/\sqrt{\beta})/\sqrt{2}$ is the annihilation operator of the "oscillator", $[\hat{b}, \hat{b}^\dagger] = 1$, and $\beta := \sqrt{8E_C/E_J}$ is the McCumber parameter. Here $\Omega := \sqrt{8E_C E_J}$ is the natural frequency of the fictitious oscillator. The factor $\beta/16$ governs the nonlinearity of the oscillator.

**ADVANCED
SCIENCE NEWS**

www.advancedsciencenews.com

**ADVANCED
QUANTUM
TECHNOLOGIES**

www.advquantumtech.com

The electric field of the cavity field affects the transmon through the gate charge n_g. The voltage between the center and ground plates given in Equation (17) leads to the coupling term

$$\hat{H}_{\text{coupling}} = g(\hat{a}^\dagger + \hat{a})(\hat{b}^\dagger + \hat{b}) \tag{22}$$

where the coupling constant is given by [9]

$$g := \frac{C_g}{C}\sqrt{2\omega E_{C_r}}, \quad E_{C_r} := \frac{e^2}{2C_r} \tag{23}$$

In typical circuits, $\Omega \approx \omega \approx 5\,\text{GHz}$ and $g \approx 300\,\text{MHz}$[6] so that the ultra-strong coupling is within the reach $(g/\omega \approx 10^{-2})$.[3,21–23]

The biggest advantage of the transmon device is that with large Josephson energy the charge dispersion is weak enough to suppress the decoherence while the sufficiently large nonlinearity, $\beta/16$, allows to selectively control transitions between different levels.[9,16] In typical applications for quantum information processing, one chooses the two lowest levels. Upon the two-level approximation, the combined circuit QED system consisting of the resonator and the transmon qubit is given by the so-called Rabi Hamiltonian

$$\hat{H}_{\text{Rabi}} = \omega\hat{a}^\dagger\hat{a} + \frac{1}{2}\Omega\hat{\sigma}^z + g(\hat{a} + \hat{a}^\dagger)\hat{\sigma}^x \tag{24}$$

So far we have ignored the photon loss of the cavity and the decoherence of the qubit. The rates of those effects are traditionally denoted by κ and γ, respectively. In conventional cavity QED, just two parameter regimes are considered, the weak-coupling $(g \lesssim \kappa, \gamma)$ and strong-coupling $(\kappa, \gamma \ll g)$ regimes, assuming that $g \ll \omega$ in realistic experiments. With superconducting circuits, while $\kappa \approx 50\,\text{MHz}$ and $\gamma \approx 1\,\text{MHz}$[10] and sufficiently smaller than other energy scales ω, Ω, and g, the coupling g can be as large as the order of ω. In circuit QED, it is thus necessary to consider a wider range of parameters and distinguish the regimes with $g \ll \sqrt{\omega\Omega}$ and $g \approx \sqrt{\omega\Omega}$. The latter is called the ultra-strong coupling regime as the word "strong coupling regime" has already been common in cavity QED. Although very difficult to reach in realistic experiments, it is also theoretically useful to consider an even stronger coupling regime (deep strong coupling regime) with $g \gg \sqrt{\omega\Omega}$.

3. Rabi Hamiltonian: Exact Properties

We have seen that the Rabi Hamiltonian

$$\hat{H} = \omega\hat{a}^\dagger\hat{a} + \frac{1}{2}\Omega\hat{\sigma}^z + g(\hat{a} + \hat{a}^\dagger)\hat{\sigma}^x \tag{25}$$

is the elementary model for the circuit QED in the ultra-strong coupling regime. The eigenstates of the Rabi Hamiltonian are usually strongly entangled states between the qubit and the cavity photons, and hence they are called the "dressed states".[31,35] In this section, we examine several features of the Rabi Hamiltonian that are valid regardless of the parameter regime, which produce interesting insights into the mathematical structure of the Rabi Hamiltonian and its eigenstates. Further properties depending on the specific parameter regimes are discussed in Section 4.

3.1. Parity Symmetry

The Rabi Hamiltonian possesses an important symmetry, that is

$$[\hat{\Pi}, \hat{H}] = 0, \hat{\Pi} := \exp(i\pi\hat{n})\hat{\sigma}^z \tag{26}$$

where $\hat{n} := \hat{a}^\dagger\hat{a}$. It is an overall number parity, and we will call it just "parity". As $\hat{\Pi}^2 = 1$, the eigenvalues of $\hat{P}$ are ± 1, which we call "even" and "odd", respectively. Note that the quadrature $\hat{X} := \hat{a} + \hat{a}^\dagger$ and $\hat{P} := -i(\hat{a} - \hat{a}^\dagger)$ of the cavity mode and the qubit flip operator $\hat{\sigma}^x$ are all odd under parity transformation

$$\hat{\Pi}\hat{X}\hat{\Pi} = -\hat{X}, \quad \hat{\Pi}\hat{P}\hat{\Pi} = -\hat{P}, \quad \hat{\Pi}\hat{\sigma}^x\hat{\Pi} = -\hat{\sigma}^x \tag{27}$$

It is useful to decompose the Hilbert space $\mathcal{H}$ into subspaces invariant under $\hat{\Pi}$, $\mathcal{H} = \mathcal{H}_e \oplus \mathcal{H}_o$. In each sector, one can choose the parity Fock basis,

$$|\Pi_n^{e/o}\rangle := (\hat{\sigma}^x)^n |n, \uparrow/\downarrow\rangle = \frac{(\hat{a}^\dagger)^n}{\sqrt{n!}}|0\rangle \otimes (\hat{\sigma}^x)^n |\uparrow/\downarrow\rangle \tag{28}$$

where we have adopted the short-hand notation $|n, \sigma\rangle := |n\rangle \otimes |\sigma\rangle$ for the product of the photon and qubit states.

It is also interesting and useful to note that within each parity subspace, the operator

$$\hat{b} := \hat{a}\hat{\sigma}^x \tag{29}$$

behaves as a canonical Bosonic operator, that is, $[\hat{b}, \hat{b}^\dagger] = 1$. It turns out that the parity Fock basis in (28) is the eigenstate of $\hat{n}_b := \hat{b}^\dagger\hat{b}$

$$\hat{n}_b |\Pi_n^{e/o}\rangle = n |\Pi_n^{e/o}\rangle \tag{30}$$

and hence the name. Naturally, it is even under parity

$$\hat{\Pi}\hat{b}\hat{P} = \hat{b} \tag{31}$$

and unlike $\hat{X}$ and $\hat{P}$, the quadratures $\hat{X}_b := \hat{b} + \hat{b}^\dagger$ and $\hat{P}_b := -i(\hat{b} - \hat{b}^\dagger)$ are all even under parity

$$\hat{\Pi}\hat{X}_b\hat{\Pi} = \hat{X}_b, \quad \hat{\Pi}\hat{P}_b\hat{\Pi} = \hat{P}_b \tag{32}$$

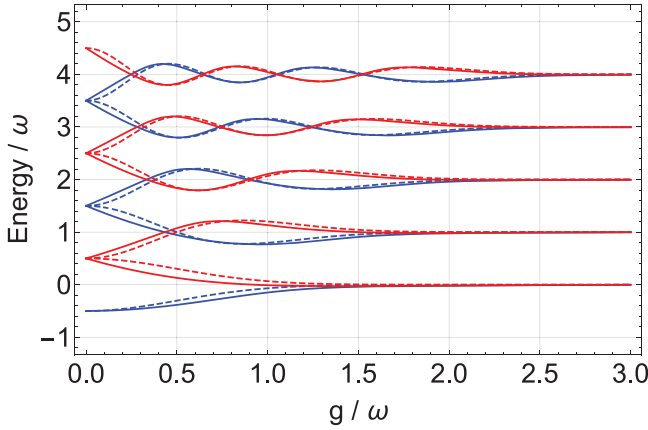### 3.2. Displaced Fock States in the Parity Basis

Here, we will develop another parity basis, which turns out to be the eigenstates of the Hamiltonian to a good approximation over an almost entire parameter range.[24,25] The relatively small error in the regime $g \approx \sqrt{\omega\Omega}$ can be further improved using the generalized rotating wave approximation described in Section 4.4.

First note that the Hamiltonian in each parity subspace is given by

$$\hat{H}_{e/o} = \omega(\hat{b} + g/\omega)^\dagger(\hat{b} + g/\omega) \pm \frac{1}{2}\Omega \exp[i\pi\hat{n}_b] \tag{33}$$

Upon the unitary transformation

$$\hat{D}_b(g/\omega)\hat{H}_{e/o}\hat{D}_b^\dagger(g/\omega) = \omega\hat{n}_b \pm \frac{1}{2}\Omega\exp(i\pi\hat{n}_b)\hat{D}_b(-2g/\omega) \tag{34}$$

**ADVANCED
SCIENCE NEWS**
www.advancedsciencenews.com

**ADVANCED
QUANTUM
TECHNOLOGIES**
www.advquantumtech.com

Figure 2. The energies of the displaced Fock states in the parity basis as a function of g (dashed lines). For comparison, the exact eigenenergies are also shown with solid lines. Here $\omega = \Omega$ has been assumed.

with the displacement operator

$$\hat{D}_b(z) := \exp(z\hat{b}^\dagger - z^*\hat{b}) \tag{35}$$

It is natural to construct a basis consisting of the displaced Fock states

$$|\tilde{\Pi}_n^{e/o}\rangle = \hat{D}_b^\dagger(g/\omega)|\Pi_b^{e/o}\rangle \tag{36}$$

Their energies are given by

$$E_n^{e/o} = n\omega + \langle\tilde{\Pi}_n^{e/o}|\,\hat{H}\,|\tilde{\Pi}_n^{e/o}\rangle = n\omega \pm (-1)^n \frac{1}{2}\Omega D_{nn}(-2g\omega) \tag{37}$$

where

$$D_{mn}(z) := \langle m|\,\hat{D}_b(z)\,|n\rangle = e^{-|z|^2/2}\sqrt{\frac{n!}{m!}}L_n^{m-n}(|z|^2)z^{m-n} \quad (m \geq n) \tag{38}$$

and $L_m^n(x)$ is the Laguerre polynomial. Interestingly, as **Figure 2** shows, the energies in Equation (37) are already close to the true eigenvalues of $\hat{H}$. In fact, they are the exact eigenstates in both $g \to 0$ and $g \to \infty$ limits. To see it, note that the matrix elements of the Hamiltonian in the basis are given by

$$\langle\tilde{\Pi}_m^{e/o}|\,\hat{H}\,|\tilde{\Pi}_n^{e/o}\rangle = \pm\frac{1}{2}\Omega D_{mn}(-2g/\omega) \tag{39}$$

For $m \neq n$, $D_{mn}(z) \to 0$ as either $|z| \to 0$ or $|z| \to \infty$. In the intermediate regime ($g \approx \sqrt{\omega\Omega}$), the matrix elements are finite and the displacement Fock states in the parity basis are not exact eigenstates. However, the matrix elements remain small compared to ω and hence they are still eigenstates of $\hat{H}^{e/o}$ to a good approximation.

We have just shown that the displaced Fock states in the parity basis in Equation (36) provide a convenient basis as a good starting point for further approximations. Nevertheless, one drawback is noted concerning the ground state: the lowest-energy state among the displaced Fock states in the parity basis is clearly a separable state. The variational wavefunctions[24,26–28]

or direct numerical calculations suggest that the ground state is an entanglement between the cavity photon and the qubit.

3.3. Exact Solution

In 2011, Braak found an analytic solution for the quantum Rabi model in the Bargmann–Fock space of analytic functions and gave the energy spectrum.[29–31] Since Braak's analytic solution, different methods were used to reproduce his result including the Bogoliubov transformation[32] and the confluent Heun functions,[33,34] and a flood of other works followed to study the analytic structure of the Rabi Hamiltonian. A detailed review on the activities in the direction is available in refs. [31, 35].

Here, we will follow ref. [32], whose presentation is more physicists friendly than Braak's original work, to summarize the analytic solution. We explicitly represent the qubit part in the eigenbasis of $\hat{\sigma}^x$, so as to rewrite the Rabi Hamiltonian in (25) into the following matrix form

$$\hat{H} = \begin{bmatrix} \omega\hat{a}^\dagger\hat{a} + g(\hat{a} + \hat{a}^\dagger) & \Omega/2 \\ \Omega/2 & \omega\hat{a}^\dagger\hat{a} - g(\hat{a} + \hat{a}^\dagger) \end{bmatrix} \tag{40}$$

In this representation, the wave function is represented by two components as

$$|\psi\rangle = \begin{bmatrix} \psi_+ \\ \psi_- \end{bmatrix} \tag{41}$$

Upon the unitary transformation $\hat{D}(g/\omega)$, where $\hat{D}(z) := \exp(z\hat{a}^\dagger - z^*\hat{a})$ with a complex number z, the Hamiltonian in Equation (40) is recast to

$$\hat{H}' = \hat{D}(g/\omega)\hat{H}\hat{D}^\dagger(g/\omega)$$
$$= \begin{bmatrix} \omega\hat{a}^\dagger\hat{a} - g^2/\omega & \Omega/2 \\ \Omega/2 & \omega\hat{a}^\dagger\hat{a} - 2g(\hat{a} + \hat{a}^\dagger) + 3g^2/\omega \end{bmatrix} \tag{42}$$

One expands the wave function in the Fock basis in the rotated frame

$$|\psi'\rangle = \begin{bmatrix} \sum_n A_n\sqrt{n}\,|n\rangle \\ \sum_n B_n\sqrt{n}\,|n\rangle \end{bmatrix} \tag{43}$$

Putting it into the eigenvalue equation

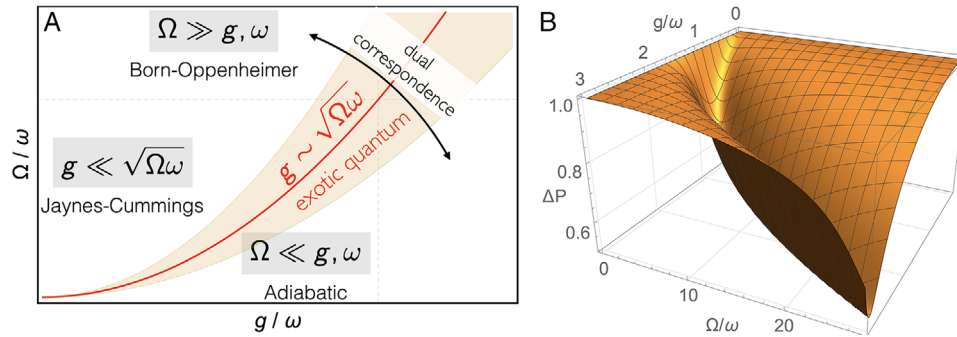$$\hat{H}'\,|\psi'\rangle = E\,|\psi'\rangle \tag{44}$$

leads to a recursion relations

$$A_n = -\frac{\Omega/2}{n\omega - g^2/\omega - E}B_n \tag{45a}$$

$$nB_n = F_{n-1}B_{n-1} - B_{n-2} \tag{45b}$$

where

$$F_n := \frac{1}{2g}\left(n\omega + \frac{3g^2}{\omega^2} - \frac{(\Omega/2)^2}{n\omega - g^2/\omega - E}\right) \tag{46}$$

ADVANCED
SCIENCE NEWS

www.advancedsciencenews.com

ADVANCED
QUANTUM
TECHNOLOGIES

www.advquantumtech.com

Figure 3. a) Interesting parameter regions and their typical characteristics of the Rabi Hamiltonian. The quantum exotic regime is around the red solid line. b) The squeezing in the ground state as shown in the standard deviation ΔP of the quadrature $\hat{P} := i(\hat{a}^\dagger - \hat{a})$. The squeezing is most pronounced in the quantum exotic regime.

One could choose the unitary transformation $\hat{D}(-g/\omega)$

$$\hat{H}'' = \hat{D}\hat{H}\hat{D}^\dagger = \begin{bmatrix} \omega\hat{a}^\dagger\hat{a} + 2g(\hat{a} + \hat{a}^\dagger) + 3g^2/\omega & \Omega/2 \\ \Omega/2 & \omega\hat{a}^\dagger\hat{a} - g^2/\omega \end{bmatrix}$$

(47)

The wave function

$$|\psi''\rangle = \begin{bmatrix} \sum_n B'_n \sqrt{n} |n\rangle \\ \sum_n A'_n \sqrt{n} |n\rangle \end{bmatrix}$$

(48)

leads to another recursion relations

$$A'_n = -\frac{\Omega/2}{n\omega - g^2/\omega - E} B'_n$$

(49a)

$$nB'_n = F_{n-1} B'_{n-1} - B'_{n-2}$$

(49b)

Now note that if the eigenvalue is not degenerate, the two wave functions should represent the same state, $|\psi'\rangle = z|\psi''\rangle$ for some complex number z. Eliminating z and noting that B_n and B'_n satisfy the same recursion relation, one can get the condition for the energy E as

$$G_\pm(E) = \sum_{n=0}^\infty B_n \left(1 \mp \frac{\Omega/2}{E + (g^2/\omega) - n\omega}\right)\left(\frac{g}{\omega}\right)^n = 0$$

(50)

The integrability of the Rabi Hamiltonian has been revealed through its analytical solution. Braak[29] has extended this approach to a generalized Rabi model with a parity breaking term $\epsilon\hat{\sigma}^x$ and found the exact solution, the first example of exact solution for a nonintegrable system. Nevertheless, the solution given above is not presented in a simple closed form. For a clearer physical insights into the Rabi Hamiltonian, various approximation methods have been developed focusing on the particular parameter regimes of physical interests.

4. Interesting Parameter Regimes

For a very simple form, the Rabi Hamiltonian exhibits surprisingly rich quantum effects. In this section, we examine various parameter regimes and interesting quantum effects that are

representative of such regimes. Although the exact solution discussed in Section 3.3 reveals the deep mathematical structure of the Rabi Hamiltonian, it is not easy to obtain physical insights into the diverse quantum effects since the solution is not given in a simple, closed form. It turns out that the individual parameter regimes allow for simple approximation methods that give direct insights into the quantum effects in particular regimes. In this section, we examine various parameter regimes of the Rabi Hamiltonian, develop relevant approximation methods, and investigate the interesting quantum effects based on the approximations.

Figure 3a provides the overall picture of the various parameter regimes and summarizes their properties in terms of the appropriate approximations. Physically, the regime around the line $2g = \sqrt{\omega\Omega}$ is the most interesting regime. As a representative example of the exotic quantum features in the regime, consider the strong squeezing effect[24] of the cavity photons as shown in Figure 3b. All other exotic quantum effects are most pronounced around the line (Section 6). On this ground, the regime around the line is called the quantum exotic regime.
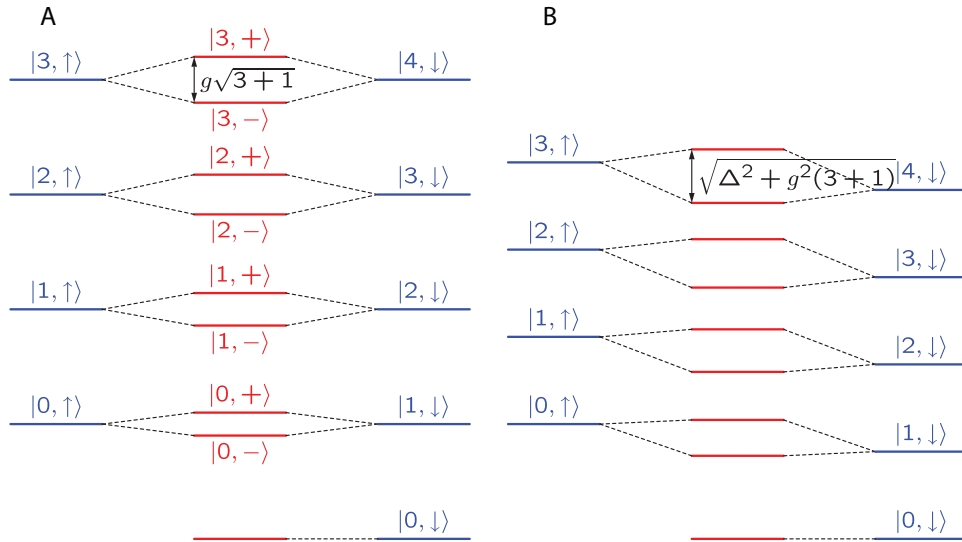
4.1. Rotating Wave Approximation ($g \ll \sqrt{\Omega\omega}$)

The most common approximation made on the Rabi Hamiltonian is the so-called rotating wave approximation (RWA). Note that the qubit-resonator coupling term can be split into to two terms

$$g(\hat{a}\hat{\sigma}^+ + \hat{a}^\dagger\hat{\sigma}^-) + g(\hat{a}\hat{\sigma}^- + \hat{a}^\dagger\hat{\sigma}^+)$$

(51)

In the first term, a quantum of energy is reduced by destroying a photon, but it is compensated by the flipping the qubit, and vice versa. On the other hand, the second term only contains processes that either simultaneously increase or decrease the energy in both the cavity and the qubit. Naturally, the latter processes occur less frequently than the former. The RWA corresponds to ignoring the second term and is supported by the above observation. This argument can be made more precise by moving to the interaction picture by the rotation

$$\hat{U}(t) = \exp\left(i\omega t\hat{a}^\dagger\hat{a} + i\Omega t\hat{\sigma}^z/2\right)$$

(52)

**ADVANCED
SCIENCE NEWS**
www.advancedsciencenews.com

**ADVANCED
QUANTUM
TECHNOLOGIES**
www.advquantumtech.com

A

B

Figure 4. Eigenstates of the Jaynes–Cummings model. a) Zero-detuning ($\Delta = 0$) case. b) Finite-detuning case.

to get

$$\hat{H}_{\text{eff}} = \hat{U}(t)\hat{H}\hat{U}^{\dagger}(t) - \hat{U}(i\partial_t \hat{U}^{\dagger})$$
$$= g(e^{-it\Delta}\hat{a}\hat{\sigma}^{+} + h.c.) + g(e^{it(\Omega+\omega)}\hat{a}\hat{\sigma}^{-} + h.c.) \quad (53)$$

where $\Delta := \omega - \Omega$ is the detuning. As typically $\omega \approx \Omega$, the second term varies much faster than the first one, and self-cancels itself. In this sense, the first term is called the rotating term and the second counter-rotating term.

Dropping the counter-rotating term, the Rabi Hamiltonian is reduced to the so-called Jaynes–Cummings (JC) Hamiltonian[36]

$$H_{\text{JC}} = \omega \hat{a}^{\dagger}\hat{a} + \frac{1}{2}\Omega\hat{\sigma}^{z} + g(\hat{a}\hat{\sigma}^{+} + \hat{a}^{\dagger}\hat{\sigma}^{-}) \quad (54)$$

The JC model has been widely used in conventional cavity QED as the coupling constant is usually very small ($g/\omega \lesssim 10^{-6}$).

Unlike the Rabi Hamiltonian, the JC Hamiltonian allows for a simple solution. This is because for each n, the state $|n, \uparrow\rangle$ is only coupled to $|n + 1, \downarrow\rangle$. Here, we have adopted a simplified notation $|n, \sigma\rangle := |n\rangle \otimes |\sigma\rangle$ for the product of the photon Fock state $|n\rangle$ ($n = 0, 1, 2, \ldots$) and the qubit logical basis state $|\sigma\rangle$. Within the subspace spanned by $|n, \uparrow\rangle$ and $|n + 1, \downarrow\rangle$ the Hamiltonian has the matrix representation of the form

$$H \doteq \begin{bmatrix} n\omega + \Omega/2 & g\sqrt{n+1} \\ g\sqrt{n+1} & (n+1)\omega - \Omega/2 \end{bmatrix} \quad (55)$$

The eigenvalues are given by

$$E_{\pm}(n) = \omega\left(n + \frac{1}{2}\right) \pm \frac{1}{2}\sqrt{(1+n)(2g)^2 + \Delta^2} \quad (56)$$

and the corresponding eigenvectors are

$$|n, +\rangle = +\cos(\theta/2)|n, \uparrow\rangle + \sin(\theta/2)|n+1, \downarrow\rangle \quad (57a)$$

$$|n, -\rangle = -\sin(\theta/2)|n, \uparrow\rangle + \cos(\theta/2)|n+1, \downarrow\rangle \quad (57b)$$

where $\tan\theta := (2g/\Delta)\sqrt{n+1}$. **Figure 4** shows the level structure of the JC model. The hybridization of the states $|n, \uparrow\rangle$ and $|n + 1, \downarrow\rangle$ is maximal at the resonance (Figure 4a), and it decreases as the detuning Δ increases (Figure 4b). It is also interesting to notice that the splitting due to the hybridization increases with n, leaving the spectrum with a irregular level spacing. This observation is important to understand the photon blockade or similar effects; see Section 6.3.

The above level structure of the eigenstates of the Jaynes–Cummings Hamiltonian can be directly observed in experiments. Consider an experiment with the spin in the excited state $|\uparrow\rangle$ and the oscillator in the number state $|n\rangle$. The probability to find the system in the state $|n + 1, \downarrow\rangle$

$$P(t) = \sin^2\left[t\Omega_n/2\right] \quad (58)$$

oscillates in time with the so-called quantum electrodynamic Rabi frequency

$$\Omega_n := \sqrt{(n+1)(2g)^2 + \Delta^2} \quad (59)$$

In particular, the frequency

$$\Omega_0 = \sqrt{(2g)^2 + \Delta^2} \quad (60)$$

describes the oscillation between $|0\rangle \otimes |\uparrow\rangle$ and $|1\rangle \otimes |\downarrow\rangle$. The effect has received great interest and has been designated with the name vacuum Rabi oscillation since it involves the the vacuum state of the cavity field, "no electromagnetic field" in some sense, casting a contrast with conventional Rabi oscillation driven by the finite electromagnetic field.
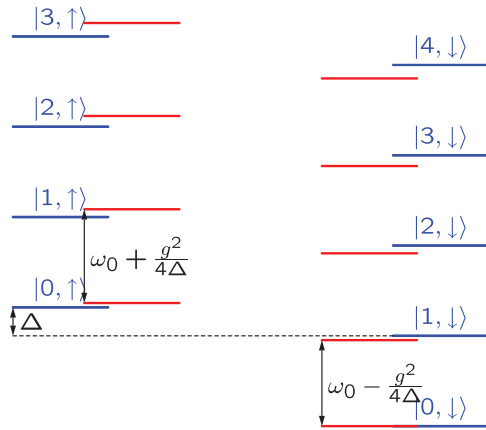
Figure 5. The energy levels of the dispersive Hamiltonian; to be compared to the energy levels of the Jaynes–Cummings model with a large detuning in Figure 4b.

4.1.1. Dispersive Regime

The large detuning limit $|\Delta| \gg g$ features further interesting properties of the JC model. To see it, consider the state $|n, \uparrow\rangle$. The only allowed transition for it is the one to $|n+1, \downarrow\rangle$. However, if the energy cost Δ for the process is bigger than the transition amplitude $g\sqrt{n+1}$, the state immediately (within the time $\approx 1/\Delta$) returns back to the original state. If the system starts in the state $|n+1, \downarrow\rangle$, the effect is similar; the transition to $|n, \uparrow\rangle$ releases energy Δ larger than $g\sqrt{n+1}$, and the reverse transition immediately pushes the system back to the state $|n+1, \downarrow\rangle$. Nevertheless, through these virtual transitions, the corresponding states obtain energy gains due to the uncertainty principle. The energy gains for $|n, \uparrow\rangle$ and $|n+1, \downarrow\rangle$ are

$$\mp \frac{g^2(n+1)}{\Delta} \tag{61}$$

respectively. In the operator form, they are described by

$$-\frac{g^2}{\Delta}\hat{a}^\dagger\hat{a}\hat{\sigma}^z - \frac{1}{2}\frac{g^2}{\Delta}\hat{\sigma}^z + (\text{constant}) \tag{62}$$

Therefore, the energy gains corresponds to the ac Stark shift, $(2g^2/\Delta)(n + 1/2)$ for the atom, or alternatively, the dispersive shift, $\sigma^z \frac{g^2}{\Delta}$ for the cavity. Overall, the effective Hamiltonian in the large detuning limit is given by

$$\hat{H}_{\text{dis}} = \left(\omega - \frac{g^2}{\Delta}\hat{\sigma}^z\right)\hat{a}^\dagger\hat{a} + \frac{1}{2}\left(\Omega - \frac{g^2}{\Delta}\right)\hat{\sigma}^z \tag{63}$$

The energy levels of the effective Hamiltonian are compared to the exact energy levels of the JC Hamiltonian in **Figure 5**. The same effective Hamiltonian can also be obtained by a unitary transformation

$$\hat{H}_{\text{dis}} = \hat{U}\hat{H}_{\text{JC}}\hat{U}^\dagger \tag{64}$$

with

$$\hat{U} = \exp\left[-\frac{g}{\Delta}(\hat{a}\hat{\sigma}^+ - \hat{a}^\dagger\hat{\sigma}^-)\right] \tag{65}$$

An important aspect of the dispersive Hamiltonian is that the qubit-cavity coupling term now commutes with the qubit and cavity Hamiltonians. This means that when the cavity is used as a probe for the quantum states of the qubit, the measurement satisfies the quantum non-demolition (QND) condition. The opposite is also true, that is, one can probe the photon states in the cavity by using the qubit as a QND probe. Such QND measurements have played crucial roles for the development of the quantum information processors based on circuit QED.[2,37–44]

4.2. Born–Oppenheimer Approximation ($\Omega \gg \omega, g$)

When the qubit transition frequency Ω is much larger than the cavity mode frequency ω and the coupling g (this is a further extreme of the dispersive regime discussed in Section 4.1.1), there is a clear separation of the time scales in the dynamics of the qubit and the cavity mode. That is, the dynamics of the qubit is so fast that the cavity field looks almost static to the qubit. This means that one can regard the cavity field variables as static parameters when solving the qubit. Diagonalizing the two by two matrix for the qubit, one obtains the two branches of the energy function

$$\hat{H}_{\text{eff}}^{\pm} = \frac{1}{2}\left[\omega(\hat{p}^2 + \hat{x}^2) \pm \sqrt{\Omega^2 + 8g^2\hat{x}^2}\right] \tag{66}$$

which is now regarded as the effective Hamiltonian for the cavity mode alone and is solved separately. Here

$$\hat{x} = \frac{\hat{a} + \hat{a}^\dagger}{\sqrt{2}}, \quad \hat{p} = \frac{\hat{a} - \hat{a}^\dagger}{i\sqrt{2}} \tag{67}$$

are the two standard quadrature variables (i.e., the "position" and "momentum" of an oscillator) for the cavity mode. The approximation just made is reminiscent of the Born–Oppenheimer approximation in solid-state physics,[45] where the splitting of time scales exists between the light and fast electrons and the heavy and slow ions.

Let us focus on the lower branch $\hat{H}_{\text{eff}}^-$, which dominates the low-energy physics. The effective potential

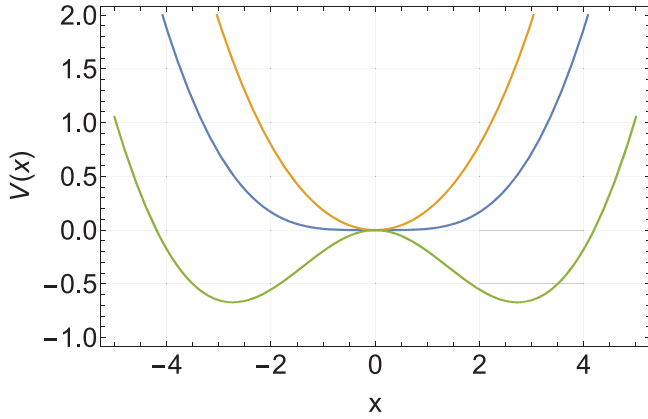$$V(x) := \frac{1}{2}\omega x^2 - \sqrt{\Omega^2 + 8g^2 x^2} \tag{68}$$

becomes bistable for $4g^2/\omega\Omega > 1$; see **Figure 6**. The minima of the effective potential is located at $\pm x_0$ given by

$$x_0^2 = \frac{1}{2}\frac{\Omega}{\omega}\left[\frac{4g^2}{\omega\Omega} - \frac{\omega\Omega}{4g^2}\right] \quad (4g^2 > \omega\Omega) \tag{69}$$

Physically, the bistability is not easy to observe as it requires the condition

$$\Omega \gg g \gg \omega \tag{70}$$

**ADVANCED
SCIENCE NEWS**

www.advancedsciencenews.com

**ADVANCED
QUANTUM
TECHNOLOGIES**

www.advquantumtech.com

Figure 6. The effective potential, $V(x)$, in Equation (68), in the Born–Oppenheimer approximation. Three representative cases are shown for $2g^2/\omega\Omega = 0.8$ (orange), 1 (blue), and 1.2 (green), respectively.

Figure 7. The approximate energies as a function of g (dashed lines) from the generalized rotating wave approximation. For comparison, the exact energies are also shown with solid lines.

However, it is still useful to analyze the bistability regime since the regime $g \gg \sqrt{\omega\Omega}$ is ultimately related to the (easier-to-reach) weak-coupling regime by the duality as we will discuss in Section 5.

4.3. Adiabatic Approximation ($\Omega \ll \omega, g$)

In the opposite limit, where $\Omega \gg \omega, g$, the separation of the time scales is pronounced again, but the slow variables are the qubit's. This regime has been previously studied by several groups in different forms.[46–49] Here we mainly follow the lines in [49].

We start with $\Omega = 0$. In this extreme case, the qubit state is completely frozen in the either eigenstate $|\pm 1\rangle$ of $\hat{\sigma}^x$. Therefore, the Hamiltonian for the cavity mode has two branches

$$\hat{H}_{\text{eff}}^{\pm} = \omega\hat{a}^{\dagger}\hat{a} \pm g(\hat{a} + \hat{a}^{\dagger}) + g^2/\omega = \omega(\hat{a} \pm g/\omega)^{\dagger}(\hat{a} \pm g/\omega) \quad (71)$$

(We have added a constant energy shift for simplicity.) It is immediately clear that the model is nothing but the shifted oscillator and the eigenstates are displaced Fock states

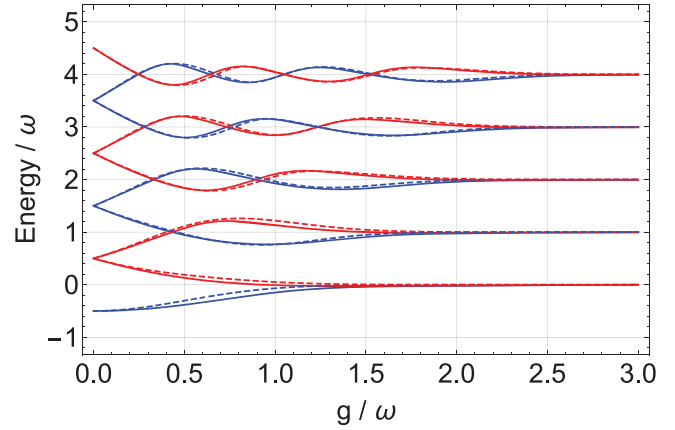$$|\tilde{n}_{\pm}\rangle := \hat{D}^{\dagger}(\pm g/\omega)|n\rangle \quad (72)$$

The overall eigenstates of the total system are thus given by $|\tilde{n}_{\pm}, \pm\rangle$ with (degenerate) eigenvalues $n\omega$.

For finite and small Ω, it causes transitions between $|m_+, +\rangle$ and $|n_-, -\rangle$. As the difference $(m - n)\omega$ in their (unperturbed) energies are bigger than Ω for $m \neq n$, the transitions are negligible. Therefore, it is sufficient to treat its effect of Ω perturbatively considering only two-by-two block spanned by $|\tilde{n}_{\pm}, \pm\rangle$

$$\begin{bmatrix} n\omega & \frac{1}{2}\Omega D_{nn}(-2g/\omega) \\ \frac{1}{2}\Omega D_{nn}(-2g/\omega) & n\omega \end{bmatrix} \quad (73)$$

where $D_{mn}(z)$ are the same as in Equation (38). The eigenstates and the corresponding eigenvalues are given by

$$|\tilde{n}_+, +\rangle \pm |\tilde{n}_-, -\rangle, \quad n\omega \pm D_{nn}(-2g/\omega)\Omega/2 \quad (74)$$

4.4. Generalized Rotating Wave Approximation

The central spirit of the rotating wave approximation is to focus on the transitions among the levels of similar energies (see Section 4.1). It has been suggested that within the spirit, one can go beyond the conventional rotating wave approximation by choosing a proper basis. Irish[50] started with the eigenbasis from the adiabatic approximation (see Section 4.3). The Hamiltonian is rewritten in the basis of the adiabatic eigenstates. Then, the argument about energy conservation that led to the RWA is applied in the new basis, and the approximate energy levels are calculated. Earlier, ref. [51] had used the same idea but they also took into account the parity conservation.

Here, we present still another approach to generalize the conventional rotating wave approximation, starting with the displaced Fock basis with a definite parity. In Section 3.2, we have seen that the displaced Fock states in the parity basis already form a good approximate eigenbasis of each parity sector $\hat{H}_{e/o}$. The small yet finite error is most pronounced around the regime $g \approx \sqrt{\omega\Omega}$. For a small $g/\sqrt{\omega\Omega}$, the displaced Fock states $|\tilde{\Pi}_{2m}^e\rangle$ and $|\tilde{\Pi}_{2m+1}^e\rangle$ form a close pair in the even parity subspace whereas such pair is formed by $|\tilde{\Pi}_{2m+1}^o\rangle$ and $|\tilde{\Pi}_{2m+2}^o\rangle$; see Equations (36) and (37). The relevant 2×2 block in each sector reads as

$$\begin{bmatrix} E_{2m}^e & \frac{1}{2}\Omega D_{2m,2m+1}(-2g/\omega) \\ \frac{1}{2}\Omega D_{2m,2m+1}(-2g/\omega) & E_{2m+1}^e \end{bmatrix} \quad (75)$$

and

$$\begin{bmatrix} E_{2m+1}^o & \frac{1}{2}\Omega D_{2m+1,2m+2}(-2g/\omega) \\ \frac{1}{2}\Omega D_{2m+1,2m+2}(-2g/\omega) & E_{2m+2}^o \end{bmatrix} \quad (76)$$

respectively, with $m = 0, 1, 2, \ldots$. Note that in this approximation, the state $|\tilde{\Pi}_0^o\rangle$ in the odd subspace is singled out (decoupled), and it gives the (approximate) ground state [with energy $-\frac{1}{2}\Omega D_{00}(-2g/\omega)$] of the Rabi Hamiltonian. The accuracy of the generalized RWA is illustrated in **Figure 7**.

**ADVANCED
SCIENCE NEWS**

www.advancedsciencenews.com

**ADVANCED
QUANTUM
TECHNOLOGIES**

www.advquantumtech.com

5. Duality

In the previous section, we have examined various parameter regimes, their properties and relations to each other. Here, we point out that both the extreme parameter regimes $g \ll \sqrt{\omega\Omega}$ and $g \gg \sqrt{\omega\Omega}$ are unitarily equivalent.[24,52] That is, when the parameter regimes in Figure 3a is folded along the line $2g = \sqrt{\omega\Omega}$, the overlapping regimes share the same properties.

Start with the limit, $g \gg \sqrt{\omega\Omega}$. In short, we will eventually make the transformation

$$\hat{H}'' = \hat{U}_y(\theta)\hat{D}(\alpha)\hat{H}\hat{D}^\dagger(\alpha)\hat{U}_y^\dagger(\theta) \tag{77}$$

Upon the displacement,

$$\hat{H}' := \hat{D}(\alpha)\hat{H}\hat{D}^\dagger(\alpha) = \omega\hat{a}^\dagger\hat{a} - \omega\alpha(\hat{a} + \hat{a}^\dagger) + g(\hat{a} + \hat{a}^\dagger)\hat{\sigma}^x$$
$$+ \frac{1}{2}\Omega\hat{\sigma}^z - 2g\alpha\hat{\sigma}^x \tag{78}$$

Combine the last two terms to get a single longitudinal term by means of the rotation $\hat{U}_y(\theta)$ with

$$\cos\theta = \frac{\Omega}{\Omega'}, \quad \sin\theta = \frac{4g\alpha}{\Omega'}, \quad \Omega' := \sqrt{\Omega^2 + (4g\alpha)^2} \tag{79}$$

$$\hat{H}'' = \hat{U}_y(\theta)\hat{H}'\hat{U}_y^\dagger(\theta) = \omega\hat{a}^\dagger\hat{a} - \omega\alpha(\hat{a} + \hat{a}^\dagger) - g\sin\theta(\hat{a} + \hat{a}^\dagger)\hat{\sigma}^z$$
$$+ g\cos\theta(\hat{a} + \hat{a}^\dagger)\hat{\sigma}^x + \frac{1}{2}\Omega'\hat{\sigma}^z \tag{80}$$

We want to remove the term

$$-\omega\alpha(\hat{a} + \hat{a}^\dagger) - g\sin\theta(\hat{a} + \hat{a}^\dagger)\hat{\sigma}^z \tag{81}$$

for the ground state $|\downarrow\rangle$, which leads to the condition

$$\omega\alpha = g\sin\theta \equiv \frac{4g^2\alpha}{\Omega'} \tag{82}$$

or equivalently

$$\frac{\Omega'}{\Omega} = \frac{4g^2}{\omega\Omega} \tag{83}$$

Putting it back into the last equation in (79),

$$\alpha = \frac{1}{2}\sqrt{\frac{\Omega}{\omega}\left(\frac{4g^2}{\omega\Omega} - \frac{\omega\Omega}{4g^2}\right)} \tag{84}$$

Note that this displacement parameter is exactly the same as the one obtained in the Born–Oppenheimer approximation, see Equation (69). Overall $\hat{H}''$ takes the same form as $\hat{H}$

$$\hat{H}'' = \omega'\hat{a}^\dagger\hat{a} + g'(\hat{a} + \hat{a}^\dagger)\hat{\sigma}^x + \frac{1}{2}\Omega'\hat{\sigma}^z + (\text{irrelevant terms}) \tag{85}$$

with renormalized parameters $\omega' = \omega$, Ω' given in (83), and g' given by

$$\frac{g'}{g} := \cos\theta = \frac{\Omega}{\Omega'} = \frac{\omega\Omega}{4g^2} \tag{86}$$

In particular, we note that the dimensionless coupling constant is renormalized

$$\frac{4g'^2}{\omega'\Omega'} = \frac{\omega\Omega}{4g^2} \to 0 \tag{87}$$

so that the effective Hamiltonian $\hat{H}''$ is now in the weak-coupling limit.

The duality picture explains why the quantum exotic regime ($g \approx \sqrt{\omega\Omega}$) is special, and it is the only regime that bears the true ultra-strong coupling physics. The duality feature is directly implied in the recurrent photon-blockade effect to be discussed in Section 6.4.

6. Exotic Quantum States in the Ultra-Strong Coupling Regime

In Sections 4, we have examined various parameter regimes and their properties. In Section 5, we have seen that the exotic quantum effects due to ultra-strong coupling is most pronounced in the so-called exotic quantum regime, where $g \approx \sqrt{\omega\Omega}$. In this section, we now survey those exotic quantum effects due to ultra-strong coupling.
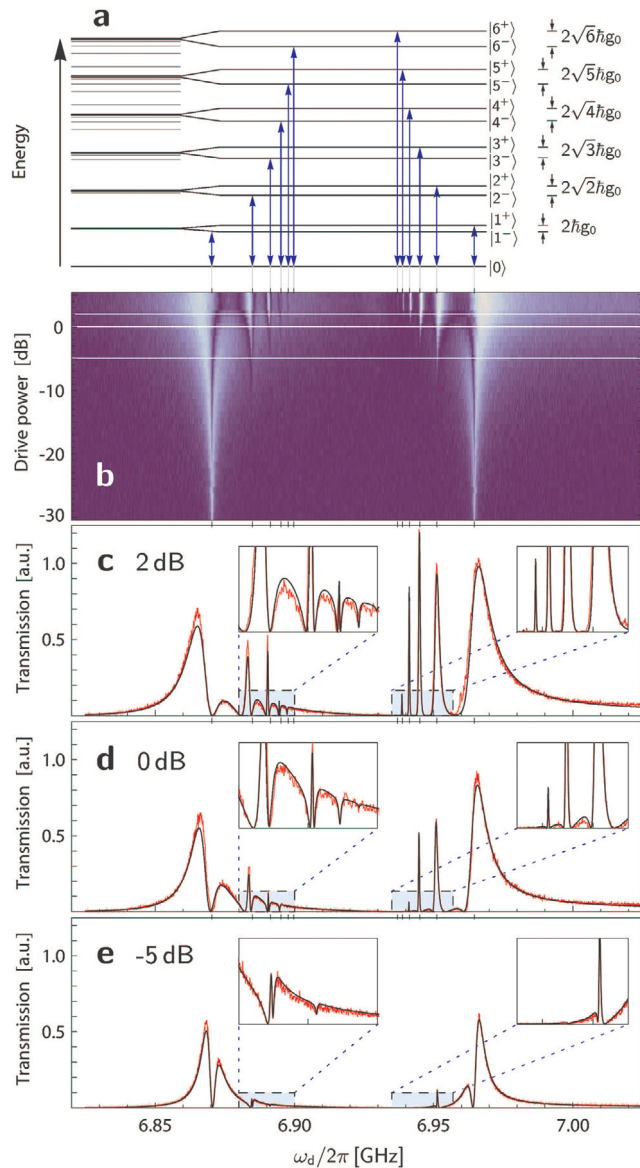
6.1. Vacuum Rabi Splitting

The first implication of the ultra-strong coupling effects in the circuit QED can be observed in the phenomenon known as the vacuum Rabi splitting, the splitting of the resonance spectral line of the vacuum Rabi oscillation into extra lines.[53]

The zero-point quantum fluctuation of the vacuum gives rise to oscillatory transitions of two-level atoms.[54] Such an effect is called the vacuum Rabi oscillation, and it is explained well by the Jaynes–Cummings (JC) model (see Section 4.1), the "weak"-coupling ($g \ll \sqrt{\omega\Omega}$) approximation of the Rabi Hamiltonian. Within the JC model, only the pairwise states $|n, \uparrow\rangle$ and $|n + 1, \downarrow\rangle$ are coupled. In particular, the state $|0, \uparrow\rangle$ involving the vacuum of the cavity mode is coupled only to $|1, \downarrow\rangle$, which results in a well-defined Rabi oscillation.

As the coupling grows stronger ($g \approx \sqrt{\omega\Omega}$), the rotating wave approximation starts to break down, and the JC model is not enough to describe the system properly in this regime. One has to take into account the counter-rotating term in Equation (51). Let us investigate the effect of the counter-rotating term perturbatively, regarding the JC model as the unperturbed Hamiltonian. The counter-rotating term induces transitions between the eigenstates of the JC Hamiltonian in Equation (57) (**Figure 8**).

Such transitions between the JC levels have been observed in spectroscopic experiments on the circuit QED system with a superconducting qubit.[53,55] The effect has also been observed with the superconducting qubit replaced by a semiconductor double quantum dot.[56,57] These experiments were performed with the coupling strengths that are not typically called as ultra strong. However, the effect comes from the counter-rotating term, and it indicates that the ultra-strong coupling effects set in.
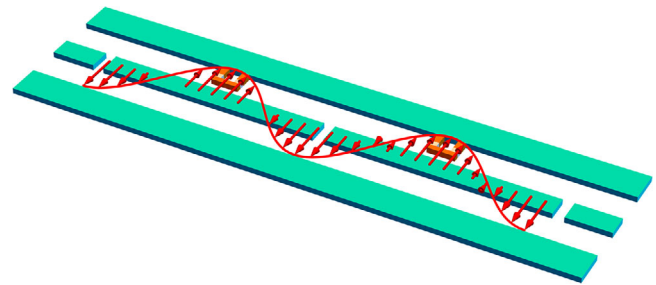
**ADVANCED
SCIENCE NEWS**

www.advancedsciencenews.com

**ADVANCED
QUANTUM
TECHNOLOGIES**

www.advquantumtech.com

Figure 8. Vacuum Rabi splitting in a circuit QED system. Reproduced with permission from Figure 3 of ref. [53]. Copyright 2009, Springer Nature.

Figure 9. Schematic of two coupled circuit QED systems. The two resonators are coupled capacitively, and the photons can tunnel from one cavity mode to another as well as interact with the two qubits. The strong photon–qubit coupling induces nonlinearity (effectively an indirect photon–photon interaction) of the cavity field, and it results in the photon-blockade effect.

through variational wavefunctions.[24,25] In passing, the ground-state squeezing should be distinguished from the squeezing effects achieved by dynamical driving.[58] In a recent experiment on superconducting circuit resonator with a large array of Josephson junctions with microwave pump, the nonlinearity of the Josephson junctions was exploited to achieve the parametric amplification and squeezed radiation.[59] The resulting squeezed radiation[60] has been used to explore the effects of the squeezed radiation on (artificial) atoms, which has until recently remained a long standing challenge in atomic physics.[61] While the dynamical approach is valuable in many applications for the coherent manipulation of quantum states and opens new possibilities (see Section 7), the ground squeezing is interesting in that it reveals the equilibrium quantum properties of circuit QED systems.

6.3. Photon Blockade

Photons themselves do not interact with each other, and in principle an infinite number of photons can occupy the same mode. However, a photon–photon interaction can be induced by the medium through light–matter interaction. A typical example is the Kerr nonlinearity induced on optical light through the medium.[54] In the circuit QED, such an indirect photon–photon interaction turns out to be repulsive and the photons already occupying a mode prevent other photons from occupying the same mode, which is called the photon-blockade effect.[62,63]

Consider two circuit QED systems coupled capacitively with each other as shown in **Figure 9**. Through the capacitor, the photons can hop from one resonator to the other. The system is described by the two JC Hamiltonians coupled with each other

$$\hat{H} = \sum_{j=L,R} \left[\omega \hat{a}_j^\dagger \hat{a}_j + \frac{1}{2}\Omega \hat{\sigma}_j^z + g(\hat{a}_j \hat{\sigma}_j^+ + h.c.) \right] + J(\hat{a}_1^\dagger \hat{a}_2 + h.c.) \quad (88)$$

where J is the photon-hopping amplitude between the two resonators and we have assumed two identical circuit QED systems for simplicity. We initially prepare a certain number of photons $N_0 \approx 10$ in one resonator and observe the evolution in time of the photon number in both resonators. In a most

6.2. Ground-State Squeezing

The ultra-strong coupling between the cavity photon and the qubit results in an entanglement to a large extent. It is common that a strong entanglement between two subsystems results in decoherence in each subsystem when observed separately. The unique feature of the photon–qubit entanglement in the circuit QED systems is that the strong entanglement makes the cavity field non-classical, that is, it leads to strong squeezing effects.

Figure 3b shows the profile in the parameter space of the standard deviation ΔP of the quadrature $\hat{P} := -i(\hat{a} - \hat{a}^\dagger)$ from exact numerical calculations. Clearly ΔP is less than the standard quantum limit $\Delta P = 1$, revealing a squeezing effect in the ground state. The ground-state squeezing can be understood

ADVANCED
SCIENCE NEWS
www.advancedsciencenews.com

ADVANCED
QUANTUM
TECHNOLOGIES
www.advquantumtech.com

simplified accounts, the dynamics can be understood by making a semiclassical approximation[62]

$$\langle \hat{a}_j \rangle =: \frac{X_j + iP_j}{2}, \quad \langle \hat{\sigma}_j^\pm \rangle = \frac{S_j^x + iS_j^y}{2}, \quad \langle \hat{\sigma}_j^z \rangle = S_j^z \tag{89}$$

where we have introduced semiclassical variables X_j, P_j, S_j^x, S_j^y, and S_j^z. The semiclassical evolution is then governed by the following set of equations

$$+\dot{X}_L = P_L - gS_L^y - JP_R \tag{90a}$$

$$-\dot{P}_L = X_L + gS_L^x - JX_R \tag{90b}$$

$$+\dot{X}_R = P_R - gS_R^y - JP_L \tag{90c}$$

$$-\dot{P}_R = X_R + gS_R^x - JX_L \tag{90d}$$

$$\dot{S}_L^x = -S_L^y - gP_L S_L^z \tag{90e}$$

$$\dot{S}_L^y = +S_L^x - gX_L S_L^z \tag{90f}$$

We choose the gauge such that

$$P_L = X_R = 0, \quad \mathbf{S}_L = (0, \sin\theta_L, \cos\theta_L), \quad \mathbf{S}_R = -(\sin\theta_R, 0, \cos\theta_R) \tag{91}$$

to get

$$\dot{X}_L = -g\sin\theta_L - JP_R \tag{92a}$$

$$\dot{P}_R = +g\sin\theta_R + JX_L \tag{92b}$$

$$\dot{\theta}_L = -gX_L \tag{92c}$$

$$\dot{\theta}_R = -gP_R \tag{92d}$$

Without the photon–qubit coupling ($g = 0$), the two resonators are just two linearly coupled harmonic oscillators. Indeed, the photon imbalance $z(t) := \langle \hat{n}_L(t) \rangle - \langle \hat{n}_R(t) \rangle = \cos(2Jt)$ oscillates with frequency $2J$. With g increasing, the oscillation becomes nonlinear, and over a critical value g_c, the oscillation frequency diverges, meaning that no photon can hop between the two resonators. Recalling that $X_j \approx P_j \approx \sqrt{N_0}$, one can expect that $g_c \approx \sqrt{N_0}$. Indeed, the numerical simulation in ref. [62] shows that $g_c \approx 2.8J\sqrt{N_0}$. The transition can be seen clearly in **Figure 10**, and the effect has been observed experimentally on a double circuit QED system.[63]

As emphasized in ref. [62], it is important to notice that the JC nonlinearity is enough to explain the photon-blockade effect. This stands in contrast with similar self-trapping effects observed in optical fibers,[64] molecules,[65] cold atom,[66–68] and polariton Bose–Einstein condensates.[69] The self-trapping in circuit QED is due to the Jaynes–Cummings nonlinearity rather than a Kerr/Bose–Hubbard-like nonlinearity.[70,71] More importantly (in our context), the prediction cannot be extended beyond the RWA, that is, the JC model. An interesting question then is what would happen if g increases even further into the ultra-strong coupling regime $g \approx \sqrt{\omega\Omega}$ or far beyond.
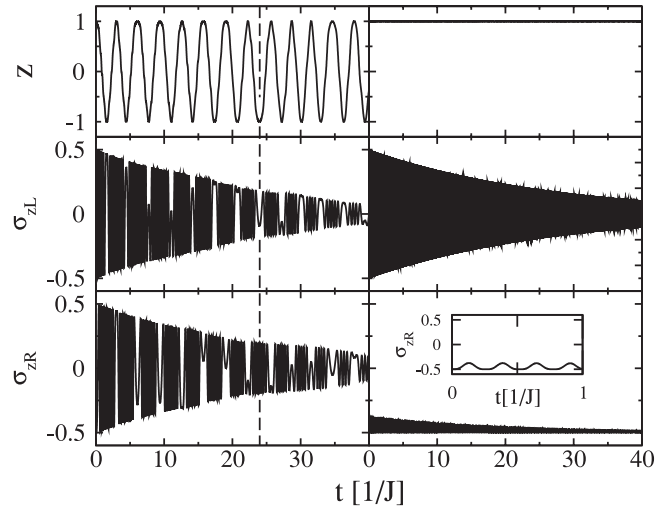
Figure 10. Photon imbalance $z(t) := \langle \hat{n}_L(t) \rangle - \langle \hat{n}_R(t) \rangle$ and the inversion of the qubits $\sigma_{zL/R}(t) := \langle \hat{\sigma}_{L/R}^z(t) \rangle$ as a function of time. Reproduced with permission from Figure 2 in ref. [62]. Copyright 2010, American Physical Society.
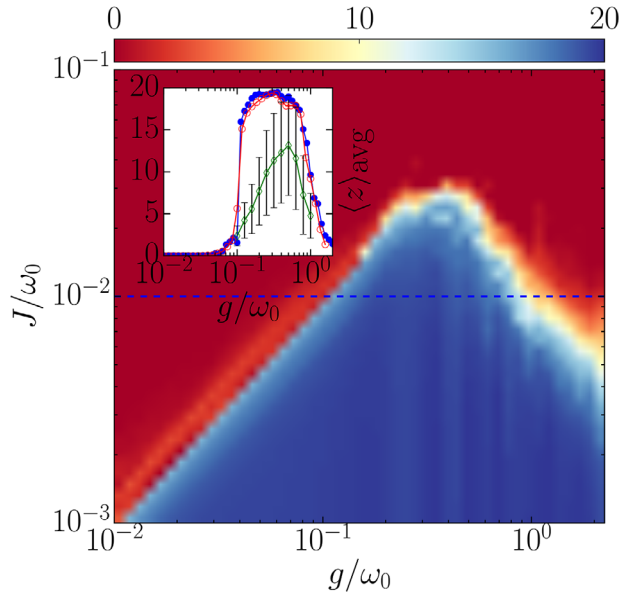
6.4. Recurrent Phase Transition

We consider again a setup of two circuit QED systems coupled capacitively with each other, as illustrated schematically in Figure 9. The photon-blockade effect in the previous section has shown an interesting consequence of the competition between the qubit-cavity coupling and the photon hopping is a self-trapping transition,[62] as recently observed in an experiment using two capacitively coupled superconducting transmission lines and transmon qubits.[63] In fact, the self-trapping transition in tunnel-coupled quantum systems can also be observed in a broad range of systems when the on-site interaction energy becomes so dominant that it prevents quantum tunneling through the tunnel barrier.[66,67,72] The photon-blockade effect can be understood along the same line: when the nonlinearity induced by the qubit-cavity coupling exceeds the inter-cavity photon hopping, the photon population dynamics undergoes a sharp transition from a delocalized (tunneling) to a localized (self-trapping) regime.[62,63]

However, that argument casts a curious observation: as shown in Section 3.2 in terms of the displaced Fock states in the parity basis, the cavity field in a circuit QED system recovers the linearity in the deep strong coupling regime $g \to \infty$. In such a regime, although difficult to reach experimentally, the photon-blockade effect should disappear. Then, what would happen if g increases into the ultra-strong coupling regime $g \approx \sqrt{\omega\Omega}$ or even further? The question cannot be answered in the semiclassical picture based on the JC model, which ignores the counter-rotating term. The latter term plays crucial roles in the ultra-strong coupling regime.

Indeed, numerical simulations and careful analyses show that the photon-blockade effect disappears and the system returns to the photon delocalization phase.[73] **Figure 11** shows the rich phase diagram across the parameter space of g and J. When the photon–qubit coupling g increases from zero, the dynamics undergoes double transitions first from a delocalized to a localized

**ADVANCED
SCIENCE NEWS**

www.advancedsciencenews.com

**ADVANCED
QUANTUM
TECHNOLOGIES**

www.advquantumtech.com

Figure 11. Phase diagram for the average photon population imbalance z_{avg} for the initial state $|20, \downarrow\rangle_L |0, \downarrow\rangle_R$. (inset) z_{avg} at $J/\omega_0 = 0.01$ for different initial states and damping conditions: The filled circle is for the Fock state $|20, \downarrow\rangle_L |0, \downarrow\rangle_R$, the empty circle for the coherent state $|\sqrt{20}, \downarrow\rangle_L |0, \downarrow\rangle_R$, and the empty diamond for $|20, \downarrow\rangle_L |0, \downarrow\rangle_R$ with finite cavity damping time $\tau_\gamma = 10^4/\omega_0$ (averaged over 300 quantum trajectories). Reproduced with permission from Figure 1 of ref. [73]. Copyright 2016, American Physical Society.

phase and then to another delocalized phase. The existence of the second transition can be understood based on the weak-strong coupling duality in the Rabi Hamiltonian that was discussed in Section 5. Just like in the weak coupling limit ($g \to 0$), the system becomes linear in the $g \to \infty$ limit, and therefore photons should eventually get delocalized again.

The recurrent photon localization–delocalization transition clearly demonstrates the competition between two qualitatively distinctive nonlinear behaviors of the circuit QED systems in the ultra-strong coupling regime: one nonlinear regime, which is commonly associated with the photon-blockade effect and is responsible for the first delocalization–localization transition, has been explored in various contexts in previous works.[74–76] However, the other nonlinear regime, responsible for the second localization–delocalization transition and the quasi-equilibration dynamics of the photon population, has been widely overlooked. Interestingly, the same picture also explains the absence of the photon blockade in the single photon transfer dynamics studied previously in ref. [77].

Another intriguing feature is that the latter phase is characterized by the quasi-equilibration of photon population, despite that the system is finite and closed.

7. Tunable Parametric Couplings

Combining with the inherent nonlinearity of the Josephson effect, the parametric modulation of the Josephson junctions in superconducting circuits provide additional tunability. It not only allows to overcome many challenging technical problems but

also offers circuit QED new opportunities to explore fundamentally new physics including strong quantum nonlinear effects that are difficult to observe using conventional quantum optical setups.[12,58] In particular, the tunable parametric coupling of qubits motivates a new QED model whose physical implications are yet to be explored.

7.1. Parametric Architectures

Tunable parametric couplings between flux qubits were originally put forward to achieve frequency selective entangling gates between otherwise weakly interacting qubits.[78,79] Recently, a great number of schemes have been proposed and experimentally demonstrated to achieve tunable parametric coupling between resonators and qubits in circuit QED.[80–87]

One noticeable direction of the efforts is the fast and accurate quantum non-demolition (QND) measurement of the quantum states.[88–90] In conventional dispersive measurement (see Section 4.1.1), although satisfying the QND, the coupling between the readout resonator and the qubit is static and weak. To fulfill high-fidelity measurements at a high speed, trade-offs between the qubit-cavity coupling and cavity-feed line coupling are required, and it often leads to additional decoherence in the system.

Another interesting direction that will be briefly discussed here is the independent control of the couplings of the rotating and counter-rotating terms in the Rabi Hamiltonian.[82,84,86] Consider a circuit QED systems with a transmon qubit and a resonator transmission line both grounded at the same node through a DC SQUID. The Josephson inductance L_g of the DC SQUID can be tuned by the external flux Φ_{ext} through the SQUID loop according to the relation

$$L_g(\Phi_{ext}) = L_0 \left| \sec\left(\pi \frac{\Phi_{ext}}{\Phi_0} \right) \right| \qquad (93)$$

where Φ_0 is the flux quantum and L_0 is the inductance scale specific to the device. As the qubit and the resonator share the same inductance L_g, the tunable inductance implies the tunable cavity-qubit coupling. The Hamiltonian for such a circuit QED system with tunable coupling is given by

$$\hat{H}(t) = \omega \hat{a}^\dagger \hat{a} + \frac{1}{2}\Omega \hat{\sigma}^z + g_1(t)(\hat{a}\hat{\sigma}^+ + h.c.) + g_2(t)(\hat{a}^\dagger \sigma^+ + h.c.) \qquad (94)$$

Here, the coupling constants of the rotating and counter-rotating terms are given by

$$g_{(1,2)} = L_g(\Phi_{ext}) \sqrt{\frac{\omega\Omega}{L_r L}} \mp \frac{C_g}{2} \sqrt{\frac{\omega\Omega}{C_r C}} \qquad (95)$$

where L and L_r are the inductance of the qubit and the resonator, respectively, and C and C_r are the respective capacitance. When the external flux through the loop of the DC SQUID loop is modulated periodically with driving frequency ω_d, the coupling constants take multiple harmonic components

$$g_{(1,2)} = g_{(1,2)}^{(0)} + \sum_n g_{(1,2)}^{(n)} \sin(n\omega_d t) \qquad (96)$$

**ADVANCED
SCIENCE NEWS**

www.advancedsciencenews.com

**ADVANCED
QUANTUM
TECHNOLOGIES**

www.advquantumtech.com

Suppose that a certain harmonic component is near the resonance with the counter-rotating process, $n\omega_n \approx \omega + \Omega$. In the interaction picture and after ignoring far-from-resonance terms in the spirit of RWA, the Hamiltonian reads as

$$\hat{H} = \omega' \hat{a}^\dagger \hat{a} + \frac{1}{2}\Omega' \hat{\sigma}^z + g'_1(\hat{a}\hat{\sigma}^+ + h.c.) + g'_2(\hat{a}^\dagger \hat{\sigma}^+ + h.c.) \qquad (97)$$

where

$$\omega' := \omega - n\omega_d/2, \quad \Omega' := \Omega - n\omega_d/2, \quad g'_1 := g_1^{(0)}, \quad g'_2 := g_2^{(n)} \qquad (98)$$

The Hamiltonian in Equation (97) looks formally similar to the Rabi Hamiltonian but with the coupling constants of the rotating and counter-rotating terms being different. We call it the generalized Rabi Hamiltonian. Another important difference of the generalized Rabi Hamiltonian is that the coupling constants g_1 and g_2 can be brought easily in the ultra-strong coupling regime $g_1, g_2 \approx \sqrt{\omega\Omega}$ with proper choice of driving frequency and resonance condition. New physical implications of the generalized Rabi Hamiltonian are discussed below.

7.2. Generalized Rabi Hamiltonian

The tunable parametric couplings between the cavity and the qubit in circuit QED introduces the generalized Rabi Hamiltonian

$$\hat{H} = \omega' \hat{a}^\dagger \hat{a} + \frac{1}{2}\Omega' \hat{\sigma}^z + g'_1(\hat{a}\hat{\sigma}^+ + h.c.) + g'_2(\hat{a}^\dagger \hat{\sigma}^+ + h.c.) \qquad (99)$$

We have kept the prime symbol in each parameter to remind that the Hamiltonian has been written in the interaction picture and that the parameters are not the bare parameters.

The physical properties of the generalized Rabi Hamiltonian in (99) has not been explored before. Here, we briefly examine one interesting feature, leaving deeper investigations for the future works.

The simplest non-trivial case is the full resonance, where $\omega' = \Omega' = 0$. In this case, the Rabi Hamilton allows an exact solution. Suppose that $g'_1 > g'_2$. Then one can take the Bogoliubov transformation

$$\hat{b} := \frac{g'_1 \hat{a} + g'_2 \hat{a}^\dagger}{\sqrt{g_1'^2 - g_2'^2}} \qquad (100)$$

The new operator $\hat{b}$ satisfies the canonical commutation relation $[\hat{b}, \hat{b}^\dagger] = 1$ for Bosons. In terms of the new Bosonic operator $\hat{b}$, the generalized Rabi Hamiltonian at the full resonance takes a simple form

$$\hat{H} = g_{\text{eff}}(\hat{b}\hat{\sigma}^+ + h.c.) \qquad (101)$$

with $g_{\text{eff}} := \sqrt{g_1'^2 - g_2'^2}$. The resulting Hamiltonian in Equation (101) is formally the same as the JC model with both cavity

and qubit frequencies vanishing. The eigenstates and their corresponding eigenvalues are given by

$$|n\rangle_b \otimes |\uparrow\rangle \pm |n+1\rangle_b \otimes |\downarrow\rangle, \quad \pm\sqrt{n}g_{\text{eff}} \qquad (102)$$

respectively, plus there is additional state exactly at the zero energy (hence, a "dark" state in some sense)

$$|D\rangle = |0\rangle_b \otimes |\downarrow\rangle \qquad (103)$$

that is, the product of the $\hat{b}$-vacuum and the ground state of the qubit. An interesting feature of the zero-energy state $|D\rangle$ is revealed when it is represented back in the basis of $\hat{a}$. Taking the inverse of the Bogoliubov transformation in (100), one can see that in the $\hat{a}$-basis, the $\hat{b}$-vacuum is a squeezed vacuum state

$$|0\rangle_b = \hat{S}(\theta/2)|0\rangle_a \qquad (104)$$

where $\hat{S}(z)$ is the unitary squeezing operator

$$\hat{S}(z) := \exp\left(\frac{1}{2}z\hat{a}^\dagger \hat{a}^\dagger - h.c.\right) \qquad (105)$$

and $\theta/2$ is the squeezing parameter determined by the relation

$$\tanh\theta = \frac{2g'_1 g'_2}{g_1'^2 + g_2'^2} \qquad (106)$$

In short, the zero-energy state $|D\rangle$ of the generalized Rabi Hamiltonian is i) always a product state regardless of the coupling strength, and ii) the cavity mode is in a squeezed vacuum state. We have observed in Section 6.2 that in general the Rabi Hamiltonian also exhibits squeezing effect. However, there is a strong entanglement between the photons and the qubit, the photons alone are in a mixed state. In the present case, the cavity mode resides in the pure-state squeezed vacuum. Recently, in ref. [59], they took advantage of the nonlinearity of Josephson junctions in a parametrically driven circuit resonator containing a large array of Josephson junctions to generate Josephson parametric amplification and squeezed microwave radiation. The method based on the zero-energy state of the generalized Rabi Hamiltonian can further facilitate the generation of squeezed microwave photons.

8. Minimal Model for Topological Qubits

In the Nature, there already exist several types of topological materials, such as topological insulators, topological superconductors, and Weyl semimetals. **Figure 12** illustrates the simplest form, the Kitaev model. However, the strengths of their coupling with single photons are very weak, because of the relatively large mode volume for conventional cavity QED and due to a large scale difference for the circuit QED. The bad controllability of the material parameters of natural topological materials causes another (and, depending on the purposes, even more serious) difficulties. For this reason, there are attempts to use an artificial topological material based on another type of synthetic spin–orbit coupling[91] where spin–orbit coupling is induced by an external
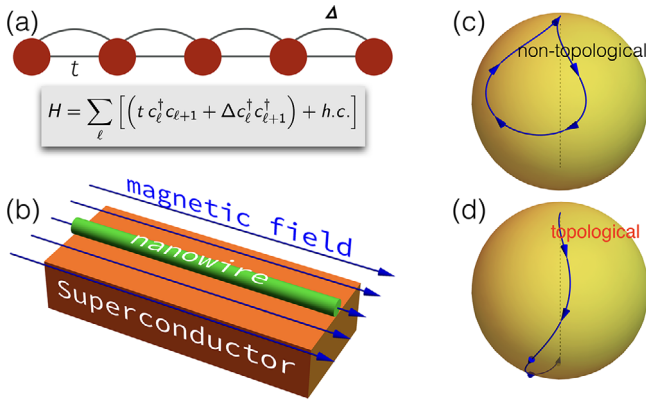
Figure 12. a) Kitaev model for 1D topological superconductor.[98] It is a 1D tight-binding model of spinless Fermions with nearest-neighbor pairing potential Δ, and difficult to realize in itself. b) A physical system, "Kitaev quantum wire", that is equivalent to the Kitaev model at low energies. It is a 1D nanowire with strong spin–orbit coupling, in proximity to a s-wave bulk superconductor, and under an external magnetic field.[99,100] c,d) Illustration of the two topologically distinct states of the Kitaev quantum wire. The arrowed lines (in blue) depict the trajectories of the electron spin on the Bloch sphere (yellow). In the non-topological state (c), the trajectory can be continuously deformed to a single point whereas it is not possible in the topological state (d).

spatially rotating (or spiraling) magnetic field. Therefore, it is desirable to devise an artificial topological matter, especially, in the form of a topological "qubit" that couples strongly with the single photons in the circuit resonator.

Recalling that the resonator in the circuit QED system is essentially a series of capacitors and inductors, as seen in Figure 1b, the artificial topological system must have large mutual capacitance or inductance. To this end, here we foremost examine the following two types of topological qubits: i) the synthetic Kitaev quantum wire (see Section 8.1 and **Figure 13** below) and ii) the Moebius Josephson ladder (see Section 8.2 and Figure 15 below). The former is a synthetic analogy of the Kitaev quantum wire (Figure 12) for the 1D topological superconductor while the latter is a direct implementation of the Moebius-strip topology in the presence of the exciton condensate. For that reason, we will put a higher priority on the Moebius Josephson ladder in this work. Both types require the fabrication of large-scale uniform Josephson junction chains, which is already available in current technology.[92–94]

There are several works on topological states of large arrays of circuit QED systems.[95–97] Here, we seek the fundamental and minimal model. In the present and next section, we will focus instead on the question: What is the smallest unit (if any) of the topological matter? More explicitly, we propose plausible and efficient methods to realize topological qubits based on the Josephson junction arrays and examine the possibility to achieve a topological QED architecture, where the topological qubit is strongly coupled to a superconducting circuit resonator, and finally, through the studies of those basic elements. Through it, we hope to explore the fundamental principle of the light–topological matter interaction. At this stage it is a progressive report rather than a complete work, and the primary spirit of the work is an utmost simplification.

8.1. Synthetic Kitaev Quantum Wire

The Kitaev model[98] for the 1D topological superconductor is the simplest model of the topological system. Being a tight-binding model of spinless Fermions with a nearest-neighbor pairing potential (see Figure 12a), it is difficult to realize in itself. A more realistic system that is equivalent at low energies has been recently proposed theoretically[99,100] and engineered experimentally.[101–103] It is based on a 1D nanowire with strong spin–orbit coupling in proximity to a conventional superconductor and under an external magnetic field (Figure 12b). We call it a "Kitaev quantum wire".

The crucial element of the Kitaev quantum wire is the spin–orbit coupling. In this work, we propose to simulate the spin–orbit coupling artificially based on the Josephson ladder and by regarding the chain index as an isospin: Consider two chains of Josephson junctions and couple them with each other via either four-way cross coupling (Figure 13a) or avoided cross coupling (Figure 13c). While the four-way junction involved in the former scheme is challenging to fabricate, it is easier to understand intuitively and hence may inspire further ideas for an experimental realization of a synthetic Kitaev chain.

One applies a proper amount of flux through each corresponding loop by means of a uniform magnetic field perpendicular to the device plane. Then, taking into account the charging energy and the Josephson tunneling of the Cooper pairs on the superconducting islands leads to the following tight-binding model

$$H = \sum_{\ell=0}^{L-1} \sum_{\sigma=\uparrow,\downarrow} \left[\epsilon_\ell b_{\ell\sigma}^\dagger b_{\ell\sigma} - t \left(b_{\ell,\sigma}^\dagger b_{\ell+1,\sigma} + h.c. \right) \right]$$
$$ - \alpha t \sum_\ell \left[\left(b_{\ell,\uparrow}^\dagger b_{\ell+1,\downarrow} - b_{\ell,\downarrow}^\dagger b_{\ell,\uparrow} \right) + h.c. \right] \tag{107}$$

where $b_{\ell,\sigma}^\dagger$ creates a Cooper pair on the ℓth site of the chain σ ($\sigma = \uparrow, \downarrow$ for the upper and lower chain, respectively). The Hamiltonian in the above equation is formally equivalent to the quantum wire with spin–orbit coupling. Two differences are i) that the chain index plays the role of isospin (α then corresponds to the dimensionless spin–orbit coupling strength) and ii) that we are dealing with Bosons (rather than Fermions). The latter does not put a serious limitation as long as the charging energy (corresponding to the large on-site repulsion for Bosons) is sufficiently large.[104] In principle, there is a wide interval from which to choose the ratio of the charging energy to the Josephson energy in the ladder. In the case where the Josephson energy is much larger than the charging energy, the tight-binding model in (107) is not valid to describe the system. However, topological properties are not affected as long as bands are well separated.

No fabrication is perfect, and one needs to carefully analyze the effects of various imperfections: First, the Josephson coupling strengths over the ladder may vary from junctions to junctions because of the junction fabrication flaws. Second, the external gate and flux may have spatial inhomogeneity. Third, the gate charge and external flux may fluctuate dynamically, causing undesirable transitions from the (topological) ground-state manifold to (non-topological) excitations. Fortunately, the system is expected to operate in the topological regime, which is robust
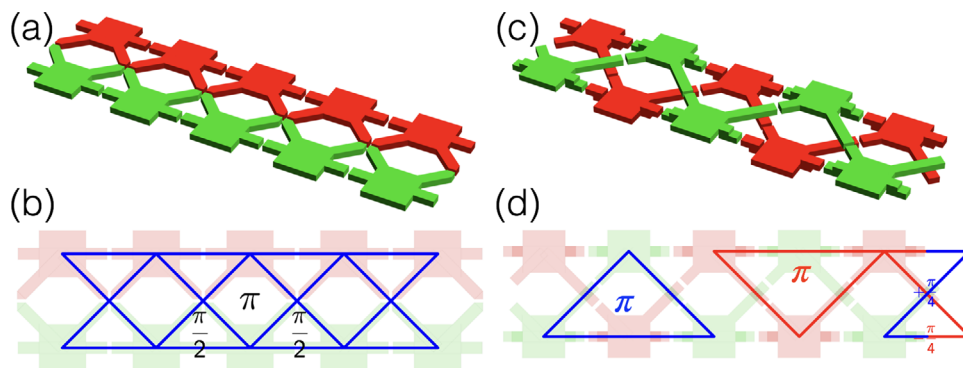
Figure 13. Two different methods to realize "synthetic spin–orbit coupling" in Josephson junction arrays in order to realize the synthetic Kitaev quantum wire (see Figure 12b). In (a) each superconducting island is Josephson coupled to the nearest neighbors as well as the next nearest neighbors. In (c), apart from the nearest-neighbor coupling along the chain, each island is Josephson coupled in zigzag manner to those belonging to different chain. Note that the superconducting islands in red and green are laid on different vertical layers. In (b) and (d), the numbers denote the required "flux angle" $\varphi := 2\pi\Phi/\Phi_0$, where Φ is the external magnetic flux threading the loop in question and $\Phi_0 := h/2e$ is the flux quantum. Both required flux angles can be easily achieved with a uniform magnetic field.
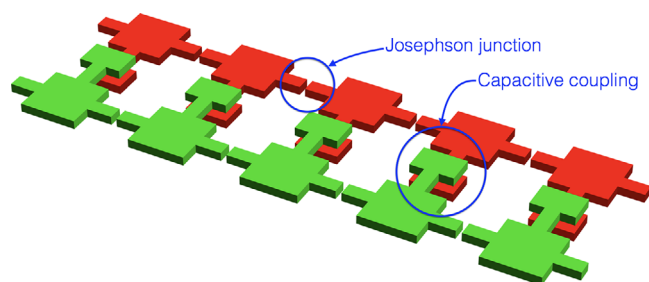

Figure 14. Schematic diagram of the capacitively coupled Josephson junction ladder with exciton condensates (superfluid). Two chains of Josephson junctions are coupled capacitively with each other. When the coupling capacitance is sufficiently large compared to the intra-chain capacitance, the elementary excitations are excitons (a particle-hole pair or, more precisely, a pair of excessive and deficit Cooper pairs). The excitons undergo a quantum phase transition from Mott insulator to superfluid as the intra-chain Josephson coupling increases. More details are referred to in refs. [105, 106].

against local fluctuations as long as the fluctuations and inhomogeneities are sufficiently small compared to the bulk energy gap. Nevertheless, with the finite bulk energy gap and temperature, those dynamical fluctuations and spatial imperfections can affect the system characteristics and need to be carefully analyzed.

8.2. Moebius Josephson Ladder

Here, we propose another type of topological qubit based on the Josephson junction array, the Moebius Josephson ladder. As explained below, it is a direct implementation of the real-space[107] Moebius-strip topology, and it will be investigated with higher priority in this work.
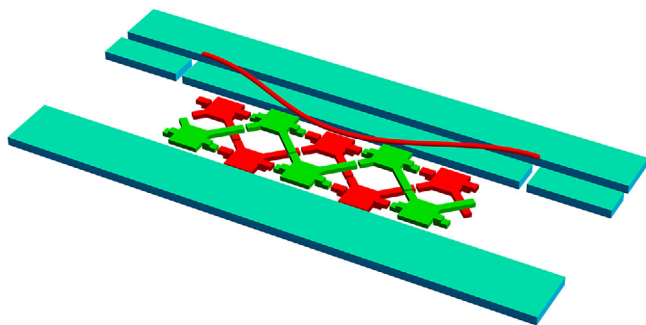
Before discussing the Moebius Josephson ladder, let us first consider the capacitively coupled Josephson ladder as shown in **Figure 14**.[92,105,106] If the coupling capacitance is sufficiently larger than the intra-chain capacitance, then the charges (either excessive or deficit Cooper pairs) in different chains across
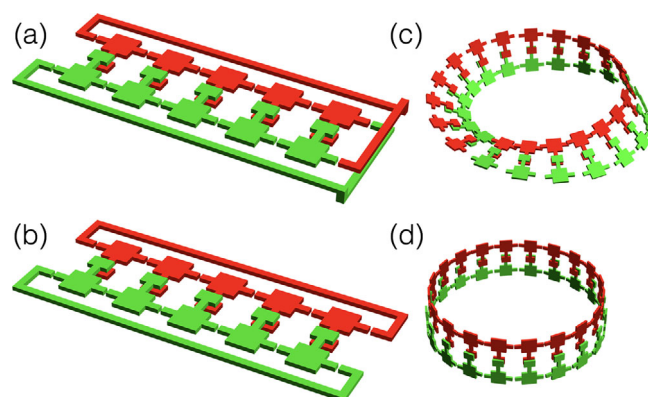
Figure 15. a) A topological qubit realized by the Moebius Josephson ladder (MJL) with twisted boundary condition (TBC). The idea was put forward by Kitaev[108,109] and built upon our own earlier works.[105,106] b) A normal Josephson ladder (JL) with a periodic boundary condition (PBC) for a comparison with the MJL. c) and d) The deformations of (a) and (b), respectively, to pronounce the topological difference between the MJL and normal JL. The MJL in (a) is considered as one of the prototypes for the "topological qubit" in this work.

the rungs are correlated. Accordingly, in such a regime the elementary excitations of the capacitively coupled Josephson ladder are "excitons", the particle-hole pairs (i.e., the pairs of excessive and deficit Cooper pairs) across the rungs of the ladder. Furthermore, as the Josephson coupling increases, the excitons undergo a quantum phase transition from the Mott insulator to the superfluid.[105,106] It is stressed that the excitons have opposite charges across each rung of the ladder, and hence the exciton superfluid implies that the supercurrents along the different chains are opposite in direction but the same in magnitude.

With a simple yet ingenious idea, Kitaev[108] has turned the capacitively coupled Josephson ladder into a topological qubit by introducing the twisted boundary condition (TBC); see **Figure 15**a. Since its real-space topological structure is identical to the celebrated Moebius strip as illustrated in Figure 15c, we call it the "Moebius Josephson ladder (MJL)".

**ADVANCED
SCIENCE NEWS**

www.advancedsciencenews.com

**ADVANCED
QUANTUM
TECHNOLOGIES**

www.advquantumtech.com

Figure 16. An example of possible coupling schemes between the synthetic Kitaev quantum wire (see Figure 13) to the superconducting circuit resonator. The electric field of the quantized microwave mode (depicted as a sine wave in red) changes dynamically the chemical potentials of the superconducting islands belonging to the, say, upper chain of the JL. As the upper and lower chain correspond to the isospin ↑ and ↓, respectively, the photon mode effectively modulates the magnetic field (and hence the topological properties) of the synthetic Kitaev quantum wire.

Figure 17. An example of possible coupling schemes between the Moebius Josephson ladder (MJL) and the superconducting circuit resonator. The electric field of the quantized microwave mode (depicted as a sine wave in red) in the resonator dynamically shifts the gate charge of a superconducting island (marked in blue) of the MJL. Properly tuning the coupling capacitance, the shift in the gate charge oscillates between $\pm e$ with the mode frequency so that the Josephson ladder (JL) is effectively switched between the MJL and the normal JL.

The measurement schemes and gate operations on the MJL for the purpose of the universal topological quantum computation have been detailed in ref. [108]. All of those gate operations are potentially useful for coupling the MJL to the circuit resonator, and certainly worth examining. In Section 9, we will examine two additional schemes based on switching between the MJL and the normal Josephson ladder with periodic boundary condition (Figure 15c,d).

Apart from its obvious advantages over the synthetic Kitaev quantum wire in Section 8.1, the MJL has one drawback: the excitation gap above the topological ground-state manifold scales as $1/L$, where L is the length of the MJL. In this work, we thus need to optimize between the excitation energy gap $\approx 1/L$ and the ground-state energy splitting $\approx \exp(-L/L_0)$; $L_0 \approx 1$. As with the synthetic Kitaev quantum wire, various imperfection effects must also be investigated.
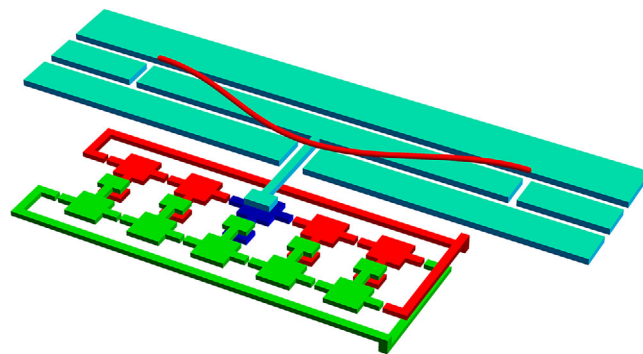
9. Light–Topological Matter Interaction

9.1. Coupling Schemes

Above, we have examined two possible prototypes for topological qubits, whose scales are macroscopic and comparable to the length of the typical superconducting circuit resonators. Now, we discuss schemes to couple them with the circuit resonator to construct topological QED systems.

In the case of the synthetic Kitaev quantum wire (Section 8.1), the idea is rather straightforward as it is a plain analogy of the Kitaev quantum wire. Putting it in the trench between the central resonator line and the ground plates (**Figure 16**), the electric field (so-called "vacuum field") of the resonator photon mode directly modulates the gate charges of one chain of the synthetic Kitaev quantum wire. Since the relative gate charges of the two chains of the synthetic Kitaev quantum wire corresponds to the external magnetic field, the photon mode can affect the topological properties of the synthetic Kitaev quantum wire.

In the case of the Moebius Josephson ladder, the coupling requires a bit more sophistication. In principle, one can exploit the gate operations on the MJL for the universal topological quantum

computations that have been proposed in ref. [108]. This is certainly worth investigating, and in this work, we will examine two additional schemes.

Figure 17 shows a scheme, where the electric field of the resonator photon mode is capacitively coupled to one single superconducting island of the MJL. By properly tuning the coupling capacitance, one can allow the field of the photon mode to modulate the gate charge of the affected island between the particle-hole symmetry point (the average gate charge $Q_g = 0$) and the maximal charge frustration point ($Q_g = e$). As the charge frustration breaks the exciton stability, the modulation effectively switches the system between the topological (MJL) phase and the normal JL phase. Therefore, unlike the coupling scheme in Figure 16 for the synthetic Kitaev chain, where the topological properties are modulated by means of model parameters, the scheme for the Moebius Josephson ladder affects the topological structure itself of the system.

Another potentially interesting scheme (not illustrated in the figure) is to put one of the long superconducting arms, which is used for the twisted boundary condition, within the circuit resonator. As pointed out by many works since the seminal work by the Yale group,[1,2] the largest coupling to the circuit resonator is achieved via inductive coupling.[93,110–112] The long superconducting arm making the twisted boundary condition may lead to an ultra-strong coupling regime or even beyond for the topological QED system.

9.2. Exploring the Fundamental Model for the Light–Topological Matter Interaction

As discussed in the earlier part of the article, conventional cavity QED systems, whose coupling is very weak, are well described by the Jaynes–Cummings (JC) model in Equation (54). Although the JC model is so simple to allow for exact analytical solutions, the implied physics is highly non-trivial. For example, the vacuum Rabi oscillation is a representative quantum phenomenon vividly illustrating the zero-point quantum fluctuations, and it has stirred many further studies.

**ADVANCED
SCIENCE NEWS**

www.advancedsciencenews.com

**ADVANCED
QUANTUM
TECHNOLOGIES**

www.advquantumtech.com

The JC model is not sufficient for the circuit QED systems because the photon–qubit coupling is very large. One has to apply the full Rabi Hamiltonian in Equation (25). For its simple form, the Rabi Hamiltonian had remained as a notoriously difficult problem until an exact solution was recently found.[29–31] Unfortunately, the exact solution is not in a closed analytic form. Accordingly, the Rabi Hamiltonian exhibits even richer and exotic quantum phenomena such as the ground-state photon squeezing, the photon blockade effect, the localization-delocalization re-entrance transition, and so on.

In contrast, there is no general theoretical model for the light–topological matter interaction. One partial reason is related to the fact that unlike the conventional phase transitions, the topological phase transitions are not described by continuous order parameters but only by discrete topological quantum numbers. On the other hand, it is clear that one can expect various combined effects implied in the Rabi Hamiltonian and the corresponding topological characteristics. We therefore hope that this work can reveal them to the extent possible.

Acknowledgements

Conflict of Interest

The author declares no conflict of interest.

Keywords

[1] A. Blais, R.-S. Huang, A. Wallraff, S. M. Girvin, R. J. Schoelkopf, *Phys. Rev. A* **2004**, *69*, 062320.

[2] A. Wallraff, D. I. Schuster, A. Blais, L. Frunzio, R.-S. Huang, J. Majer, S. Kumar, S. M. Girvin, R. J. Schoelkopf, *Nature* **2004**, *431*, 162.

[3] T. Niemczyk, F. Deppe, H. Huebl, E. P. Menzel, F. Hocke, M. J. Schwarz, J. J. Garcia-Ripoll, D. Zueco, T. Hummer, E. Solano, A. Marx, R. Gross, *Nat. Phys.* **2010**, *6*, 772.

[4] M. Trif, Y. Tserkovnyak, *Phys. Rev. Lett.* **2012**, *109*, 257002.

[5] A. Cottet, T. Kontos, B. Douçot, *Phys. Rev. B* **2013**, *88*, 195415.

[6] R. J. Schoelkopf, S. M. Girvin, *Nature* **2008**, *451*, 664.

[7] S. Haroche, J.-M. Raimond, *Exploring the Quantum: Atoms, Cavities, and Photons*, Oxford University Press, Oxford, UK **2006**.

[8] H. Walther, B. T. H. Varcoe, B.-G. Englert, T. Becker, *Rep. Prog. Phys.* **2006**, *69*, 1325.

[9] J. Koch, T. M. Yu, J. Gambetta, A. A. Houck, D. I. Schuster, J. Majer, A. Blais, M. H. Devoret, S. M. Girvin, R. J. Schoelkopf, *Phys. Rev. A* **2007**, *76*, 042319.

[10] A. A. Houck, D. I. Schuster, J. M. Gambetta, J. A. Schreier, B. R. Johnson, J. M. Chow, L. Frunzio, J. Majer, M. H. Devoret, S. M. Girvin, R. J. Schoelkopf, *Nature* **2007**, *449*, 328.

[11] F. Arute, K. Arya, R. Babbush, D. Bacon, J. C. Bardin, R. Barends, R. Biswas, S. Boixo, F. G. S. L. Brandao, D. A. Buell, B. Burkett, Y. Chen, Z. Chen, B. Chiaro, R. Collins, W. Courtney, A. Dunsworth, E. Farhi, B. Foxen, A. Fowler, C. Gidney, M. Giustina, R. Graff, K. Guerin, S. Habegger, M. P. Harrigan, M. J. Hartmann, A. Ho, M. Hoffmann, T. Huang, *Nature* **2019**, *574*, 505.

[12] A. Blais, S. M. Girvin, W. D. Oliver, *Nat. Phys.* **2020**, *16*, 247.

[13] Y. Nakamura, Y. A. Pashkin, J. S. Tsai, *Nature* **1999**, *398*, 786.

[14] Chiorescu, Y. Nakamura, C. J. P. M. Harmans, J. E. Mooij, *Science* **2003**, *299*, 1869.

[15] J. M. Martinis, S. Nam, J. Aumentado, C. Urbina, *Phys. Rev. Lett.* **2002**, *89*, 117901.

[16] D. Vion, A. Aassime, A. Cottet, P. Joyez, H. Pothier, C. Urbina, D. Esteve, M. H. Devoret, *Science* **2002**, *296*, 886.

[17] H. Paik, D. I. Schuster, L. S. Bishop, G. Kirchmair, G. Catelani, A. P. Sears, B. R. Johnson, M. J. Reagor, L. Frunzio, L. I. Glazman, S. M. Girvin, M. H. Devoret, R. J. Schoelkopf, *Phys. Rev. Lett.* **2011**, *107*, 240501.

[18] M. M. Desjardins, J. J. Viennot, M. C. Dartiailh, L. E. Bruhat, M. R. Delbecq, M. Lee, M.-S. Choi, A. Cottet, T. Kontos, *Nature* **2017**, *545*, 71.

[19] K. D. Petersson, L. W. McFaul, M. D. Schroer, M. Jung, J. M. Taylor, A. A. Houck, J. R. Petta, *Nature* **2012**, *490*, 380.

[20] P.-B. Li, Y.-C. Liu, S.-Y. Gao, Z.-L. Xiang, P. Rabl, Y.-F. Xiao, F.-L. Li, *Phys. Rev. Appl.* **2015**, *4*, 044003.

[21] J. Bourassa, J. M. Gambetta, J. A. A. Abdumalikov, O. Astafiev, Y. Nakamura, A. Blais, *Phys. Rev. A* **2009**, *80*, 032109.

[22] J. Bourassa, F. Beaudoin, J. M. Gambetta, A. Blais, *Phys. Rev. A* **2012**, *86*, 013814.

[23] P. Nataf, C. Ciuti, *Phys. Rev. Lett.* **2011**, *107*, 190402.

[24] M.-J. Hwang, M.-S. Choi, *Phys. Rev. A* **2010**, *82*, 025802.

[25] M.-J. Hwang, M.-S. Choi, *Phys. Rev. B* **2013**, *87*, 125404.

[26] H. B. Shore, L. M. Sander, *Phys. Rev. B* **1973**, *7*, 4537.

[27] H. Chen, Y.-M. Zhang, X. Wu, *Phys. Rev. B* **1989**, *40*, 11326.

[28] J. Stolze, L. Müller, *Phys. Rev. B* **1990**, *42*, 6704.

[29] D. Braak, *Phys. Rev. Lett.* **2011**, *107*, 100401.

[30] D. Braak, *Ann. Phys.* **2013**, *525*, L23.

[31] D. Braak, in *Proceedings of the Forum of Mathematics for Industry 2014* (Ed: R. S. Anderssen), Springer, New York **2015**, pp. 75–92.

[32] Q.-H. Chen, C. Wang, S. He, T. Liu, K.-L. Wang, *Phys. Rev. A* **2012**, *86*, 023822.

[33] H. Zhong, Q. Xie, M. T. Batchelor, C. Lee, *J. Phys. A: Math. Theor.* **2013**, *46*, 415302.

[34] A. J. Maciejewski, M. Przybylska, T. Stachowiak, *Phys. Lett. A* **2014**, *378*, 3445.

[35] Q. Xie, H. Zhong, M. T. Batchelor, C. Lee, *J. Phys. A: Math. Theor.* **2017**, *50*, 113001.

[36] E. T. Jaynes, F. W. Cummings, *Proc. IEEE* **1963**, *51*, 89.

[37] A. Wallraff, D. I. Schuster, A. Blais, L. Frunzio, J. Majer, M. H. Devoret, S. M. Girvin, R. J. Schoelkopf, *Phys. Rev. Lett.* **2005**, *95*, 060501.

[38] M. Boissonneault, J. M. Gambetta, A. Blais, *Phys. Rev. A* **2008**, *77*, 060305.

[39] M. Boissonneault, J. M. Gambetta, A. Blais, *Phys. Rev. A* **2009**, *79*, 013819.

[40] M. Boissonneault, J. M. Gambetta, A. Blais, *Phys. Rev. Lett.* **2010**, *105*, 10.

[41] D. Zueco, G. M. Reuther, S. Kohler, P. Hänggi, *Phys. Rev. A* **2009**, *80*, 033846.

[42] E. Jeffrey, D. Sank, J. Mutus, T. White, J. Kelly, R. Barends, Y. Chen, Z. Chen, B. Chiaro, A. Dunsworth, A. Megrant, P. J. J. O'Malley, C. Neill, P. Roushan, A. Vainsencher, J. Wenner, A. N. Cleland, J. M. Martinis, *Phys. Rev. Lett.* **2014**, *112*, 190504.

[43] L. C. G. Govia, A. A. Clerk, *New J. Phys.* **2017**, *19*, 023044.

**ADVANCED
SCIENCE NEWS**

www.advancedsciencenews.com

**ADVANCED
QUANTUM
TECHNOLOGIES**

www.advquantumtech.com

[44] T. Walter, P. Kurpiers, S. Gasparinetti, P. Magnard, A. Potočnik, Y. Salathé, M. Pechal, M. Mondal, M. Oppliger, C. Eichler, A. Wallraff, *Phys. Rev. Appl.* **2017**, *7*, 054020.

[45] M. Born, R. Oppenheimer, *Ann. Phys.* **1927**, *389*, 457.

[46] S. Schweber, *Ann. Phys.* **1967**, *41*, 205.

[47] R. Graham, M. Höhnerbach, *Z. Phys. B: Condens. Matter* **1984**, *57*, 233.

[48] M. D. Crisp, *Phys. Rev. A* **1992**, *46*, 4138.

[49] E. K. Irish, J. Gea-Banacloche, I. Martin, K. C. Schwab, *Phys. Rev. B* **2005**, *72*, 195410.

[50] E. K. Irish, *Phys. Rev. Lett.* **2007**, *99*, 173601.

[51] I. D. Feranchuk, L. I. Komarov, A. P. Ulyanenkov, *J. Phys. A* **1996**, *29*, 4035.

[52] M.-J. Hwang, R. Puebla, M. B. Plenio, *Phys. Rev. Lett.* **2015**, *115*, 180404.

[53] L. S. Bishop, J. M. Chow, J. Koch, A. A. Houck, M. H. Devoret, E. Thuneberg, S. M. Girvin, R. J. Schoelkopf, *Nat. Phys.* **2009**, *5*, 105.

[54] R. Loudon, *The Quantum Theory of Light*, 3rd ed., Oxford University Press, Oxford, UK **2000**.

[55] L. S. Bishop, *Ph.D. Thesis*, Yale University, **2010**.

[56] H. Toida, T. Nakajima, S. Komiyama, *Phys. Rev. Lett.* **2013**, *110*, 066802.

[57] A. Wallraff, A. Stockklauser, T. Ihn, J. R. Petta, A. Blais, *Phys. Rev. Lett.* **2013**, *111*, 249701.

[58] P. D. Nation, J. R. Johansson, M. P. Blencowe, F. Nori, *Rev. Mod. Phys.* **2012**, *84*, 1.

[59] M. A. Castellanos-Beltran, K. D. Irwin, G. C. Hilton, L. R. Vale, K. W. Lehnert, *Nat. Phys.* **2008**, *4*, 929.

[60] D. Toyli, A. Eddins, S. Boutin, S. Puri, D. Hover, V. Bolkhovsky, W. Oliver, A. Blais, I. Siddiqi, *Phys. Rev. X* **2016**, *6*, 031004.

[61] K. W. Murch, S. J. Weber, K. M. Beck, E. Ginossar, I. Siddiqi, *Nature* **2013**, *499*, 62.

[62] S. Schmidt, D. Gerace, A. A. Houck, G. Blatter, H. E. Türeci, *Phys. Rev. B* **2010**, *82*, 100507.

[63] J. Raftery, D. Sadri, S. Schmidt, H. E. Türeci, A. A. Houck, *Phys. Rev. X* **2014**, *4*, 031043.

[64] S. M. Jensen, *IEEE J. Quantum Electron.* **1981**, *QE-18*, 1580.

[65] J. Eilbeck, P. Lomdahl, A. Scott, *Phys. D* **1985**, *16*, 318.

[66] A. Smerzi, S. Fantoni, S. Giovanazzi, S. R. Shenoy, *Phys. Rev. Lett.* **1997**, *79*, 4950.

[67] M. Albiez, R. Gati, J. Fölling, S. Hunsmann, M. Cristiani, M. K. Oberthaler, *Phys. Rev. Lett.* **2005**, *95*, 402.

[68] S. Levy, E. Lahoud, I. Shomroni, J. Steinhauer, *Nature* **2007**, *449*, 7162 579.

[69] D. Sarchi, I. Carusotto, M. Wouters, V. Savona, *Phys. Rev. B* **2008**, *77*, 12.

[70] I. Zapata, F. Sols, A. J. Leggett, *Phys. Rev. A* **2003**, *67*, 021603.

[71] M. Trujillo-Martinez, A. Posazhennikova, J. Kroha, *Phys. Rev. Lett.* **2009**, *103*, 105302.

[72] M. Abbarchi, A. Amo, V. G. Sala, D. D. Solnyshkov, H. Flayac, L. Ferrier, I. Sagnes, E. Galopin, A. Lemaître, G. Malpuech, J. Bloch, *Nat. Phys.* **2013**, *9*, 275.

[73] M.-J. Hwang, M. S. Kim, M.-S. Choi, *Phys. Rev. Lett.* **2016**, *116*, 153601.

[74] A. Imamoglu, H. Schmidt, G. Woods, M. Deutsch, *Phys. Rev. Lett.* **1997**, *79*, 1467.

[75] K. M. Birnbaum, A. Boca, R. Miller, A. D. Boozer, T. E. Northup, H. J. Kimble, *Nature* **2005**, *436*, 87.

[76] A. Ridolfo, M. Leib, S. Savasta, M. J. Hartmann, *Phys. Rev. Lett.* **2012**, *109*, 193602.

[77] S. Felicetti, G. Romero, D. Rossini, R. Fazio, E. Solano, *Phys. Rev. A* **2014**, *89*, 013853.

[78] P. Bertet, C. J. P. M. Harmans, J. E. Mooij, *Phys. Rev. B* **2006**, *73*, 064512.

[79] A. O. Niskanen, K. Harrabi, F. Yoshihara, Y. Nakamura, S. Lloyd, J. S. Tsai, *Science* **2007**, *316*, 723.

[80] M. S. Allman, F. Altomare, J. D. Whittaker, K. Cicak, D. Li, A. Sirois, J. Strong, J. D. Teufel, R. W. Simmonds, *Phys. Rev. Lett.* **2010**, *104*, 177004.

[81] M. Allman, J. Whittaker, M. Castellanos-Beltran, K. Cicak, F. da Silva, M. DeFeo, F. Lecocq, A. Sirois, J. Teufel, J. Aumentado, R. W. Simmonds, *Phys. Rev. Lett.* **2014**, *112*, 123601.

[82] Y. Chen, C. Neill, P. Roushan, N. Leung, M. Fang, R. Barends, J. Kelly, B. Campbell, Z. Chen, B. Chiaro, A. Dunsworth, E. Jeffrey, A. Megrant, J. Y. Mutus, P. J. J. O'Malley, C. M. Quintana, D. Sank, A. Vainsencher, J. Wenner, T. C. White, M. R. Geller, A. N. Cleland, J. M. Martinis, *Phys. Rev. Lett.* **2014**, *113*, 220502.

[83] M. R. Geller, E. Donate, Y. Chen, M. T. Fang, N. Leung, C. Neill, P. Roushan, J. M. Martinis, *Phys. Rev. A* **2015**, *92*, 012320.

[84] D. C. McKay, S. Filipp, A. Mezzacapo, E. Magesan, J. M. Chow, J. M. Gambetta, *Phys. Rev. Appl.* **2016**, *6*, 064007.

[85] R. K. Naik, N. Leung, S. Chakram, P. Groszkowski, Y. Lu, N. Earnest, D. C. McKay, J. Koch, D. I. Schuster, *Nat. Commun.* **2017**, *8*, 1904.

[86] Y. Lu, S. Chakram, N. Leung, N. Earnest, R. Naik, Z. Huang, P. Groszkowski, E. Kapit, J. Koch, D. I. Schuster, *Phys. Rev. Lett.* **2017**, *119*, 15.

[87] M. Reagor, C. B. Osborn, N. Tezak, A. Staley, G. Prawiroatmodjo, M. Scheer, N. Alidoust, E. A. Sete, N. Didier, M. P. da Silva, E. Acala, J. Angeles, A. Bestwick, M. Block, B. Bloom, A. Bradley, C. Bui, S. Caldwell, L. Capelluto, R. Chilcott, J. Cordova, G. Crossman, M. Curtis, S. Deshpande, T. El Bouayadi, D. Girshovich, S. Hong, A. Hudson, P. Karalekas, K. Kuang, et al., *Sci. Adv.* **2018**, *4*, eaao3603.

[88] N. Didier, J. Bourassa, A. Blais, *Phys. Rev. Lett.* **2015**, *115*, 203601.

[89] N. Didier, E. A. Sete, M. P. da Silva, C. Rigetti, *Phys. Rev. A* **2018**, *97*, 022330.

[90] E. A. Sete, A. Galiautdinov, E. Mlinar, J. M. Martinis, A. N. Korotkov, *Phys. Rev. Lett.* **2013**, *110*, 210501.

[91] J. Klinovaja, D. Loss, *Phys. Rev. X* **2013**, *3*, 011008.

[92] H. Shimada, P. Delsing, *Phys. Rev. Lett.* **2000**, *85*, 3253.

[93] V. E. Manucharyan, J. Koch, L. I. Glazman, M. H. Devoret, *Science* **2009**, *326*, 113.

[94] V. E. Manucharyan, N. A. Masluk, A. Kamal, J. Koch, L. I. Glazman, M. H. Devoret, *Phys. Rev. B* **2012**, *85*, 024521.

[95] B. M. Anderson, R. Ma, C. Owens, D. I. Schuster, J. Simon, *Phys. Rev. X* **2016**, *6*, 041043.

[96] Y.-P. Wang, W.-L. Yang, Y. Hu, Z.-Y. Xue, Y. Wu, *npj Quantum Inf.* **2016**, *2*, 16015.

[97] W. Nie, Y.-x. Liu, *Phys. Rev. Res.* **2020**, *2*, 2.012076.

[98] A. Y. Kitaev, *Phys.-Usp.* **2001**, *44*, 131.

[99] J. Alicea, Y. Oreg, G. Refael, F. von Oppen, M. P. A. Fisher, *Nat. Phys.* **2011**, *7*, 412.

[100] J. Alicea, *Rep. Prog. Phys.* **2012**, *75*, 076501.

[101] V. Mourik, K. Zuo, S. M. Frolov, S. R. Plissard, E. P. A. M. Bakkers, L. P. Kouwenhoven, *Science* **2012**, *336*, 1003.

[102] A. Das, Y. Ronen, Y. Most, Y. Oreg, M. Heiblum, H. Shtrikman, *Nat. Phys.* **2012**, *8*, 887.

[103] S. Nadj-Perge, I. K. Drozdov, J. Li, H. Chen, S. Jeon, J. Seo, A. H. MacDonald, B. A. Bernevig, A. Yazdani, *Science* **2014**, *346*, 602.

[104] In 1D space, there is no essential distinction among Fermions, (hard-core) Bosons, and spins, and indeed there are Wigner–Jordan transformations from one to another.

[105] M.-S. Choi, M. Y. Choi, T. Choi, S.-I. Lee, *Phys. Rev. Lett.* **1998**, *81*, 4240.

[106] M. Lee, M.-S. Choi, M. Y. Choi, *Phys. Rev. B* **2003**, *68*, 506.

[107] On the contrary, most of the topological materials studied in the literature involve the momentum-space topology.

[108] A. Kitaev, arXiv:cond-mat/0609441, **2006**.

[109] A. Kitaev, G. W. Moore, K. Walker, arXiv:0706.3410, **2007**.

[110] L. B. Nguyen, Y.-H. Lin, A. Somoroff, R. Mencia, N. Grabon, V. E. Manucharyan, *Phys. Rev. X* **2019**, *9*, 041041.

[111] R. Kuzmin, N. Mehta, N. Grabon, R. Mencia, V. E. Manucharyan, *npj Quantum Inf.* **2019**, *5*, 20.

[112] V. E. Manucharyan, *Ph.D. Thesis*, Yale University, **2012**.

Mahn-Soo Choi is a professor of physics at Korea University in South Korea. He studied at POSTECH and acquired his Ph.D. in physics in 1998. After a postdoctoral fellowship at the University of Basel in Switzerland and a research fellowship at Korea Institute for Advanced Study, he joined the Faculty of Physics at Korea University in 2002. He started his research career in condensed matter theory, and expanded his interest to quantum computation and quantum information theory. He has been working on mesoscopic transport, spin qubits in quantum dots, superconducting qubits, the superconducting circuit QED, and related quantum hybrid systems.